UNIVERSIDADE FEDERAL DE SÃO CARLOS
CENTRO DE CIÊNCIAS EXATAS E DE TECNOLOGIA
PROGRAMA DE PÓS-GRADUAÇÃO EM CIÊNCIA E ENGENHARIA DE MATERIAIS

EXPLORING MULTIPHASIC MULTI PRINCIPAL ELEMENT ALLOYS: AN APPROACH USING EXPERIMENTAL AND COMPUTATIONAL TOOLS

Flávio Fávaro de Assis

São Carlos-SP
2025

UNIVERSIDADE FEDERAL DE SÃO CARLOS
CENTRO DE CIÊNCIAS EXATAS E DE TECNOLOGIA
PROGRAMA DE PÓS-GRADUAÇÃO EM CIÊNCIA E ENGENHARIA DE MATERIAIS

EXPLORING MULTIPHASIC MULTI PRINCIPAL ELEMENT ALLOYS: AN APPROACH USING EXPERIMENTAL AND COMPUTATIONAL TOOLS

Flávio Fávaro de Assis

Master Thesis submitted to the Graduate Program in Materials Science and Engineering as a partial requirement for obtaining the degree of MASTER IN MATERIALS SCIENCE AND ENGINEERING

Supervisor: Dr. Francisco Gil Coury
Co Supervisor: Dr. Pedro Henrique Fernandes de Oliveira
Funding Agency: FAPESP - Grant: 2023/12712-7 (01/11/2023 – 31/10/2025)

São Carlos-SP
2025

VITAE

Bachelors in Materials Engineering from the Federal University of São Carlos (2023).

Folha de Aprovação

Defesa de Dissertação de Mestrado do candidato Flávio Favaro de Assis, realizada em 29/01/2026.

Comissão Julgadora:

Prof. Dr. Francisco Gil Coury (UFSCar)

Prof. Dr. Guilherme Zepon (UFSCar)

Prof. Dr. Witor Wolf (USP)

O Relatório de Defesa assinado pelos membros da Comissão Julgadora encontra-se arquivado junto ao Programa de Pós-Graduação em Ciência e Engenharia de Materiais.

AKNOWLEDGMENTS

I acknowledge my supervisor, Professor Francisco Gil Coury, and co-supervisor, Pedro Oliveira, for the opportunity to work with both and for all their help, advice, patience, and guidance, without which this work simply would not have been possible.

I thank my girlfriend, Bárbara, for all her affection, warmth, encouragement, partnership, understanding, and patience during this very challenging period. I thank my family, especially my mother, Rosa Maria, my brother, Francisco Fávaro, and my uncle, José Luis, for all their help and support during these two years of work.

My Acknowledgement to Professor Pedro Moreira from the Physics Department of UFSCar for innumerous insights and valuable provided throughout the DFT calculations and the interpretation of computational simulation results.

I also thank my friends from UFSCar: all the members of the mezzanine and the LCE team, where I completed my internship. I especially thank Gabriela Bugni, for helping me "unblock" the work progress numerous times, Argos Soares, for countless conversations about perspectives and graduate studies, and Gustavo Bertoli and David Silva for their help and tips on diffraction data processing, phase fraction analysis, and article suggestions.

Finally, I thank my childhood friends: Bonela, Giovanni, João, Zé, Messias, Pedro, Halak, Vitor, and Will, for the long journey we have shared together, amidst doubts and difficult times, always keeping the bond between us intact.

My acknowledgments to the financing agencies that supported this work: To FAPESP - Fundação de Amparo à pesquisa do estado de São Paulo for the financial support provided for this work through a scholarship, process number 2023/12712-7. CAPES and FAPESP. This study was financed in part by the Coordenação de Aperfeiçoamento de Pessoal de Nível Superior - Brasil (CAPES) - Finance Code 001.

ABSTRACT

High entropy alloys (HEAs) are a class of metals that do not have a single principal element in their composition. Initially great effort was made to search for single phase HEAs but with the development of more recent frameworks, great interest emerged around multiphasic microstructures. In this study, two different routes aim to search phase stability and structural properties involving multiphasic HEAs. The first study investigates phase stability of the $Cr_{51.5}Co_{15}Ni_{33.5}$ duplex HEA. This alloy was designed using CALPHAD simulations to achieve a dual-phase microstructure of Face-Centered Cubic (FCC) and Body-Centered Cubic (BCC) phases, while suppressing the formation of the detrimental sigma phase. The HEA was characterized using SEM, TEM, XRD and synchrotron diffraction. Experimental results confirmed the presence of the FCC and BCC phases, although the formation of the sigma phase was also observed, consistent with TSAI´s criteria and warranting further analysis of the CALPHAD predictions. The second Chapter shows a combination of simulation techniques and experimental analysis to estimate interfacial energies of a HEA based on Ni superalloys. The composition of the HEA was designed by high throughput calculations to have thermal stability at high temperature and a microstructure composed of FCC matrix and $L1_2$ Ni_3Al-type precipitates. The main simulation technique employed was Density Functional Theory – DFT trough the code Quantum Espresso using the supercell method. The results obtained were compared to experimental analysis of synchrotron x-ray diffraction data and precipitation simulations showing that the combination of techniques can lead to reasonable values of interfacial energy. That combination of methods serves as a starting point to develop reliable methodologies for estimating interfacial energies for metallic alloys, which is important since that energies between FCC and L12 in superalloys and HEAs are difficult to measure experimentally and play a key role in phase stability and final properties of the material.

Keywords: High-Entropy Alloys; Superalloys; Precipitation Hardening; DFT; Duplex

RESUMO

EXPLORANDO LIGAS DE ELEMENTO MULTIPRINCIPAL MULTIFÁSICAS: UMA ABORDAGEM USANDO FERRAMENTAS EXPERIMENTAIS E COMPUTACIONAIS

O primeiro estudo analisa a estabilidade de fases da HEA duplex $Cr_{51.5}Co_{15}Ni_{33.5}$. Essa liga foi projetada por simulações CALPHAD para obter uma microestrutura bifásica composta por fases cúbica de face centrada (CFC) e cúbica de corpo centrado (CCC), suprimindo a formação da fase sigma, considerada prejudicial. A HEA foi caracterizada por MEV, MET, DRX e difração de síncrotron. Os resultados experimentais confirmaram a presença das fases CFC e CCC, embora também tenha sido observada a formação da fase sigma, em concordância com os critérios de Tsai, indicando a necessidade de análise adicional das previsões CALPHAD. O segundo capítulo combina simulações e análises experimentais para estimar energias interfaciais de uma HEA baseada em superligas de níquel. Sua composição foi projetada por cálculos de alto desempenho para garantir estabilidade térmica em alta temperatura e uma microestrutura composta por matriz CFC e precipitados $L1_2$ do tipo Ni_3Al. A principal técnica de simulação foi a Teoria do Funcional da Densidade (DFT) no código Quantum Espresso, usando o método de supercélulas. Os resultados foram comparados com dados experimentais de difração de raios X de síncrotron e simulações de precipitação, mostrando que a combinação de métodos pode fornecer valores razoáveis de energia interfacial. Isso é relevante porque tais energias (entre CFC e $L1_2$) são difíceis de medir experimentalmente e têm papel central na estabilidade de fases e nas propriedades finais do material.

Keywords: Ligas de alta entropia; Superligas; Endurecimento por Precipitação; DFT; Duplex.

INDEX

Pg.
APPROVAL PAGE i
AKNOWLEDGMENTS ii
ABSTRACT iii
RESUMO v
INDEX vii
CHAPTER 1 – INTRODUCTION 1
CHAPTER 2 – PRODUCTION AND CHARACTERIZATION OF A DUPLEX MULTICOMPONENT ALLOY. 3
2.1 INTRODUCTION 3
2.2 MATERIALS AND METHODS 4
2.2.1 COMPOSITION DESIGN 4
2.2.2 PRODUCTION OF SAMPLES 5
2.2.3 MICROSCOPY ANALYSIS 5
2.2.4 X-RAY DIFFRACTION ANALYSIS 6
2.2.5 NANOINDENTATION TESTS 7
2.3 RESULTS AND DISCUSSION 8
2.3.1 THERMODYNAMIC CALCULATIONS 8
2.3.2 XRD ANALYSIS 10
2.3.3 OPTICAL AND SCANNING ELECTRON MICROSCOPY ANALYSIS .. 13
2.3.4 TRANSMISSION ELECTRON MICROSCOPY 20
2.3.5 NANOINTENTATION ANALYSIS 23
2.4 CONCLUSIONS 25
CHAPTER 3 – EXPLORING INTERFACIAL ENERGY MODELLING FOR $L1_2$ PRECIPITATION HARDENED HEAS 27
3.1 INTRODUCTION 27
3.2 LITERATURE REVIEW 30
3.2.1 SUPERALLOYS 30
3.2.2 EXTENDING SUPERALLOY FEATURES TO HEAS 31
3.2.3 PHYSICAL METALLURGY OF SUPERALLOYS 33
3.2.4 ABOUT THE MAIN TYPES OF PRECIPITATES IN SUPERALLOYS .. 38

3.2.5 PRECIPITATION KINECTICS.....41
3.2.6 DENSITY FUNCTIONAL THEORY.....44
3.3 MATERIALS AND METHODS..... 54
3.4 RESULTS AND DISCUSSION 61
3.5 CONCLUSIONS 75
CHAPTER 4 – FINAL DISCUSSION AND CONCLUSIONS 77
4.1 CONCLUSIONS 77
4.2 SUGGESTIONS FOR FUTURE WORKS..... 78
REFERENCES..... 80

CHAPTER 1 – INTRODUCTION

The development of metallic alloys has evolved significantly over the last century, driven by the constant demand for materials capable of operating under increasingly severe service conditions. From steels to metallic glasses, progress in alloy design has enabled the optimization of properties such as mechanical strength, corrosion resistance, thermal stability, and toughness. Among the most notable metallurgical advancements are Ni-based superalloys [10], whose outstanding strength and oxidation resistance at high temperatures have made them strategic materials in aerospace propulsion systems [4], power generation, and other critical technologies [16].

More recently, the emergence of high-entropy alloys (HEAs), also referred to as multi-principal element alloys, has expanded conventional alloy design paradigms. Unlike traditional alloys, which are typically formulated around a single main element, HEAs contain multiple principal elements in near-equiatomic proportions [1]. This compositional strategy allows the formation of solid-solution matrices with significant chemical complexity, resulting in unique combinations of mechanical and physical properties. While early studies focused predominantly on single-phase solid-solution HEAs, subsequent research revealed that multiphase HEAs could exhibit superior mechanical performance through mechanisms such as precipitation strengthening, transformation-induced plasticity (TRIP), and twinning-induced plasticity (TWIP) [26].

Within this context, special attention has been devoted to CrCoNi-based HEAs due to their remarkable toughness and deformation behavior at low stacking-fault energy levels. In parallel, the concept of high-entropy superalloys (HESAs) has emerged, integrating the foundational principles of superalloys—such as ordered precipitate strengthening—with the chemical complexity of multi-component alloys. This hybrid design approach aims to combine the excellent toughness of HEAs with the creep resistance and high-temperature stability of conventional Ni-based superalloys [12].

Given these developments, the present work investigates multiphase HEAs through two complementary approaches. In the first part, a duplex CrCoNi-based alloy was designed using thermodynamic simulations to target a dual-phase FCC+BCC microstructure and after that, experimentally produced for analysis. Its microstructural evolution and mechanical response were evaluated to understand the strengthening effects arising from the coexistence of multiple phases. In the second part, a precipitation-strengthened HEA with $L1_2$-type precipitates was studied, and density functional theory (DFT) calculations were performed to estimate interfacial energies between the matrix and ordered phases. These values were then employed to support precipitation modeling in CALPHAD-based simulations, enabling a combined experimental-computational analysis relevant to high-temperature multiphase HEAs.

CHAPTER 2 – PRODUCTION AND CHARACTERIZATION OF A DUPLEX MULTICOMPONENT ALLOY.

2.1 INTRODUCTION

Multiprincipal Element Alloys (MPEAs), also known as High Entropy Alloys (HEAs), are metallic alloys that have multiple principal elements rather than a single dominant one [1]. These alloys, often described as concentrated solid solutions [2], [3] have attracted attention due to their good of properties such as tenacity and strength [4-8]. HEAs have demonstrated potential in applications related to various kinds of features, such as cryogenic properties [9], [10], corrosion resistance [11], high-temperature environments [12], [13] and superconductivity [14], [15]. HEAs potential applications include electrocatalysis and the nuclear industry [22], [23], as well as biomedical uses, such as prostheses and implants [24], [25].

The fact that those materials do not have a single principal element leads to a gigantic number of possible alloys and to the possibility of attending to various demands. Furthermore, computational methodologies can be very important to facilitate HEA design [16- 21]

To date, various combinations of elements have been utilized to create HEAs. Among the most successful are transition metals from the 3d family, with the CrCoNi alloy system receiving considerable attention. Within the broader category of HEAs, CrCoNi alloys have emerged as a standout system due to their exceptional mechanical properties. Previous results show that these alloys exhibit some of the highest values of fracture toughness ever reported [26]. Such properties can be attributed to mechanisms such as Twinning-Induced Plasticity (TWIP) [26] and Transformation-Induced-Plasticity (TRIP) that occur on low stacking fault energy (SFE) compositions, which is well illustrated by Bertoli et al. [35]. Furthermore, CrCoNi alloys also feature excellent corrosion resistance, being able even to outperform conventional materials like 304 stainless steels in acidic environments [22],[23].

Studies to develop duplex structures within HEAs have gained attention because such microstructural features can optimize the balance between

strength and ductility. A combination of body-centered cubic phase (BCC) and face centered cube (FCC) phases are already well-known in conventional materials, such as duplex stainless steels, and their application to HEAs has shown similar promise. For example, duplex AlCoCrFeNi alloys have demonstrated excellent mechanical performance, while studies of VCrCoFe alloys have highlighted the benefits of dual-phase structures in achieving high strength [27]-[30].

In the Cr-Ni case, as it will be shown, the BCC phase is very Cr-rich, which may lead to a strong, however low ductility phase, which is characteristic of pure Cr [37]. Some studies indeed report good mechanical properties and a positive reinforcing effect of the bcc phase on duplex binary Cr-Ni alloys [38]. Despite the well-documented benefits of the CrCoNi system, to our knowledge no research has been conducted on the development of duplex CrCoNi alloys combining both face-centered cubic (FCC) and body-centered cubic (BCC) phases. However, there are studies that show that Co helps suppress the brittle-to-ductile transition in Cr, improving overall ductility [39] Studies indicate that Co contents of at least 30 at. % can effectively lower the brittle-to-ductile transition temperature of Cr to below room temperature, which could result in an improved Cr-Co-Ni duplex alloy over binary Cr-Ni [39].

This chapter builds on CALPHAD calculations to design and produce a duplex CrCoNi alloy. The chosen alloy composition, $Cr_{51.5}Co_{15}Ni_{33.5}$ should contain a strong but still ductile BCC phase and a low stacking fault energy FCC phase as well as no deleterious phases such as the sigma phase.

2.2 MATERIALS AND METHODS

2.2.1 COMPOSITION DESIGN

Thermodynamic calculations were performed to identify compositions suitable for achieving a duplex structure. These calculations were performed using CALPHAD method trough two different software: Thermo-Calc® and Pandat®, using, respectively the databases TCHEA3 for Thermo-Calc® and PANHEA2022 for Pandat®. CrCoNi isotherms and isopleths diagrams were built. Those provided relevant insights into phase stability of the alloy.

2.2.2 PRODUCTION OF SAMPLES

The specimens for this study were produced using a Buhler GmbH AM model electric arc furnace equipped with a high-vacuum chamber. During the fabrication process, an argon atmosphere was maintained inside the furnace to prevent contamination. Chromium, cobalt, and nickel of commercial purity (99.9% or above) were used as the base elements, and three distinct samples were produced. One sample was studied in its as-cast condition and will be named simply “as-cast”. The second sample underwent a homogenization treatment at 1100°C for 6 hours in an EDG-furnace and then was called in water to achieve uniform microstructure and composition without forming sigma phase (according to CALPHAD predictions). Due to the absence of controlled atmosphere or vacuum system in the EDG-furnace, the sample was encapsulated in a quartz tube under vacuum to prevent oxidation during heat treatment. The material that underwent homogenization will be referred to as “homogenized sample.”

2.2.3 MICROSCOPY ANALYSIS

Before any characterization process, the material in both conditions, as-cast and homogenized underwent metallographic preparation. The samples were submitted to metallographic preparation, including mounting in Bakelite, grinding with SiC papers ranging from 180 to 2000 grit, and polishing using aluminum oxide (alumina). Subsequently, the samples were etched with aqua regia for approximately 45 seconds and then cleaned under running water.

The samples underwent detailed microstructural characterization using optical microscopy (OM), scanning electron microscopy (SEM), and transmission electron microscopy (TEM). Initially a Shimadzu optical microscope was used to determine the number of phases in the alloy and estimate their fractions. 12 Images of each sample were captured by OM. The images were taken from at least 5 different regions of each sample. For each image, phase fraction measurements were conducted using superficial analysis, and the final phase fraction of phases in one sample was calculated as the average of all 12 measurements. Such image analysis was made using the software ImageJ. This

procedure provided an initial understanding of the two phases present in the microstructure of each sample.

For more detailed imaging and analysis, a Phillips XL-30 FEG scanning electron microscope was employed. High-magnification images in secondary electron (SE) and backscattered electron (BSE) modes were obtained, enabling better characterization of the material's phases. Energy-dispersive spectroscopy (EDS) analyses were also conducted to compare the elemental composition of the phases with data predicted by CALPHAD simulations. Composition maps were generated, offering valuable insights into the distribution of elements across different regions of the samples. Further SEM analysis were performed using electron backscattered diffraction (EBSD) technique with a TESCAN – MIRA-2 electron microscope. EBSD analysis was performed to study the alloy microstructure and differentiate its phases from a crystallographic point of view.
Transmission electron microscopy (TEM) analyses were performed using TECNAI-FEG and TECNAI-LaB6 microscopes, both located at the Laboratory of Characterization and Structure (LCE) and operating at 200kV. These analyses included imaging, compositional mapping, and electron diffraction pattern acquisition.

2.2.4 X-RAY DIFFRACTION ANALYSIS

To identify the phases present and confirm their crystalline structures, X-ray diffraction (XRD) analysis was performed using a Bruker D8 Advance ECO diffractometer. The instrument operated with a Cu-Kα1 characteristic emission line (wavelength 1.54 Å, 8.047 keV). Scans were conducted over a 2θ range of 5° to 120°, providing comprehensive data on the phases within the produced samples.

In addition to conventional laboratory XRD, synchrotron XRD was utilized to obtain higher resolution data and gather additional structural information. This experiment was made at Petra III, DESY, in Germany. The parameters used in this analysis were the following: it was used a Perkin Elmer 2d Detector and monochromatic X-ray beam at 87kev generated with a crystal monochromator.

The distance between sample and detector was 1.226m and the beam area was 700 x 700 μm². The analysis was made under transmission mode. This technique provided higher resolution and confirmed the findings from the previous analysis.

2.2.5 NANOINDENTATION TESTS

Since dealing with a duplex alloy, nanoindentation tests were made to evaluate the separate hardness of the two present phases in the material, as well other mechanical properties such as elastic modulus and yielding stress. The homogenized sample was subject to a series of 50 indentations, whereas only the indentations which fully fell on the FCC or on the BCC phases were analyzed. The interface indentations were discarded. A total of 8 indentation fell fully at the BCC phase, whereas 25 indentations fell in the FCC.

For the tests a Berkovich tip was used, aligned to a load of 10 mN. The loading and unloading rate were set for 0,25 mN/min. The maximum load was maintained for 10 s. The hardening was determined as the ratio between the load and the maximum indented area. To obtain the elastic modulus, the Oliver and Phaar [32] method was used.

To obtain more information using nano hardness test, different models were analyzed to extract the hardening coefficient of a nanoindentation curve, as well the yielding stress. To obtain the former one, the model used by Qiao [33] was applied. The results obtained by the model were used as input in the model proposed by Gao [34], which provides an estimation for the yielding stress of each phase. The later model is exhibited in Equation 1, where H, E, α, n and Y are respectively the measured hardness and elastic modulus, the effective cone angle for the Berkovich tip (19,7º), the hardening coefficient and the yielding stress.

$$\frac{H}{Y} = \frac{2}{3}\left[\left(1 - \frac{1}{n}\right) + \left(\frac{3}{4} + \frac{1}{n}\right)\left(\frac{1}{3}\frac{E}{Y}tan\,(\alpha)\right)^{n}\right]$$

2.3 RESULTS AND DISCUSSION

2.3.1 THERMODYNAMIC CALCULATIONS

Using CALPHAD calculations via Pandat® software (PANHEA2023 database), the stability of phases for CrCoNi alloys was studied. As shown in figure 2.1, which represents an isotherm of $Cr_{51.5}Co_{15}Ni_{33.5}$ at 1100°C shows that the alloy lies on a field which exhibits FCC + BCC phases.

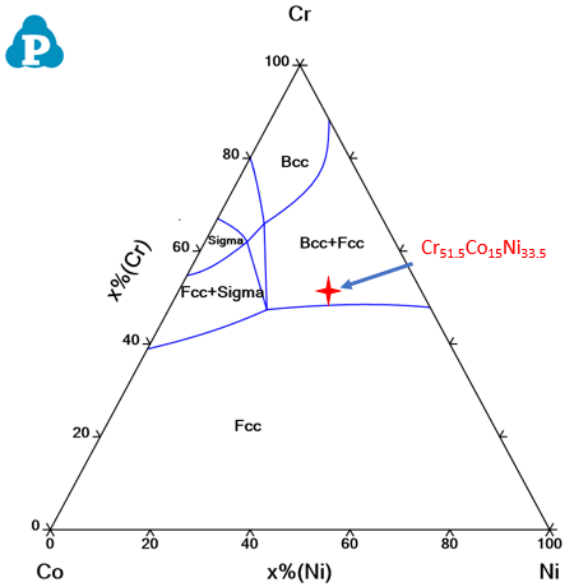

Figure 2.1: isotherms of CrCoNi ternary phase diagram at 1100oC. The alloy´s composition is indicated by the star, in the duplex FCC+BCC phase field.

The calculations showed that $Cr_{51,5}Co_{15}Ni_{33,5}$ HEA would exhibit a duplex structure while not forming sigma phase. Therefore, the mentioned composition is appropriate to form duplex structure without sigma. Another way to visualize these compositional field is through the isopleth shown in Figure 2.2, which illustrates the phases present as temperature and the Ni and Cr content in the alloy vary from 0 to 85 at%, while keeping the Co composition fixed at 15 at%. As seen in Figure 2.2, the isopleth also allows that for the selected composition, the sigma phase would not form in this alloy. Another interesting feature concerning the mentioned alloy is that it is a pseudo-eutectic alloy.

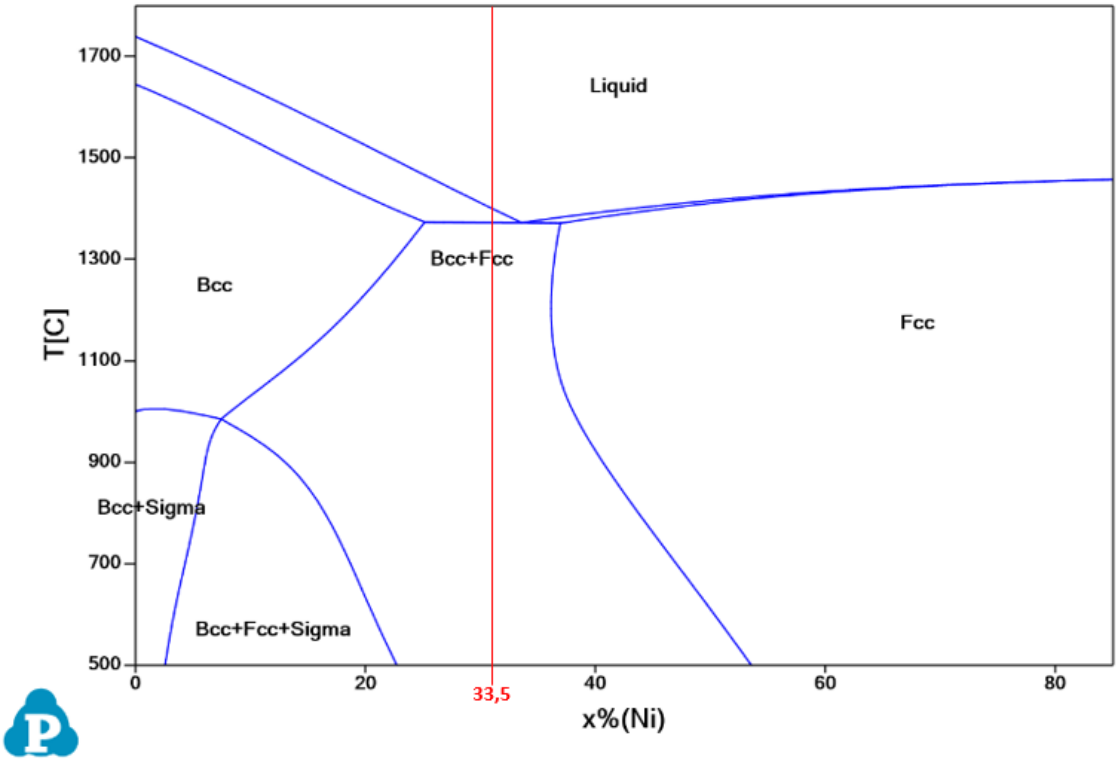

Figure 2.2: isopleth of CrCoNi maintaining Co content fixed at 15 at% and varying Ni (and Cr) from 0% to 85%. The figure allows to observe that no sigma would be formed for this composition even at low temperatures.

The phase fraction for FCC and BCC phases of $Cr_{51,5}Co_{15}Ni_{33,5}$ HEA at different temperatures were calculated using the PANHEA2022 database. Those fractions are shown in tables 2.1. The composition of both phases was also calculated and are shown in table 2.2. The temperatures shown in tables 2.1 and 2.2 are close to the chosen homogenization temperature of the alloy and present the maximum and minimum temperatures when solid phases and liquid coexist.

Table 2.1: phase fractions of BCC and FCC phases for temperatures close to the homogenization temperature.

T °C	Present Phases	Fraction of BCC	Fraction of FCC
1370	BCC & FCC	0.28	0.72
1100	BCC & FCC	0.12	0.88

Table 2.2: atomic composition of BCC and FCC phases in temperatures close to the homogenization temperature

T °C	Present Phases	%Cr in BCC	%Co in BCC	%Ni in BCC	%Cr in FCC	%Co in FCC	%Ni in FCC
1370	BCC & FCC	60.35	13.51	26.14	47.99	15.59	36.42
1100	BCC & FCC	73.80	10.48	15.72	48.52	15.60	35.87

The calculations presented in the tables above are essential for the design of the material used in this work. Additionally, using CALPHAD, it was possible to estimate the composition of the sigma phase at temperatures below 1000°C, predicted to be 61.30 at% Cr, 21.30 at% Ni, and 17.4 at% Co.

2.3.2 XRD ANALYSIS

Figure 2.3(a), displays the diffraction pattern for the as-cast sample, revealing a limited number of peaks. This is likely due to the presence of a small number of large grains in the material, a typical feature of the as-cast condition, when it is expected that the grains are bigger than they would be after some heat treatment as recrystallization. A similar pattern is observed in the diffractogram of the homogenized sample, shown in Figure 2.3(b).

The diffraction pattern in 2.3(a) indicates the presence of the peaks related to BCC and FCC phases. This provides strong evidence for the coexistence of these two phases in this sample and supports the presence of a duplex microstructure across the different processing conditions.

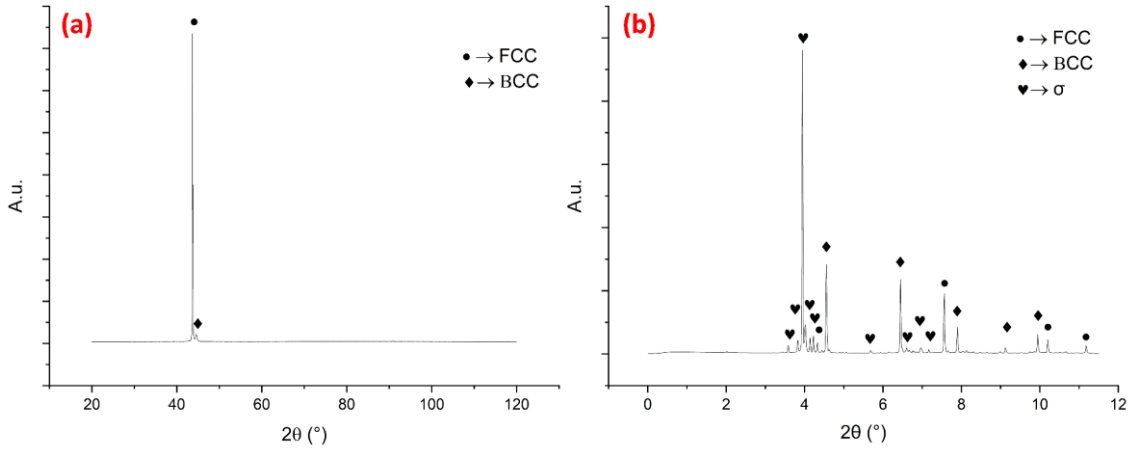

Figure 2.3: Indexed x-ray diffraction patterns using a cu-k-a radiation for sample "as-cast" (a) and synchrotron radiation for homogenized sample (b).

In Figure 2.3(b), the presence of BCC and FCC diffraction peaks in the synchrotron diffraction pattern of the homogenized sample is more evident, confirming the presence of these phases. Based on these observations across both diffractograms, there is substantial evidence supporting the presence of this duplex structure in the as-cast $Cr_{51.5}Co_{15}Ni_{33.5}$ HEA.

However, it is noteworthy that Figure 2.3 (b) also reveals additional peaks around 2 $2\theta \approx 45°$, suggesting the presence of the sigma phase. These peaks indicate that, despite efforts to minimize its formation, the sigma phase seems to be present in homogenized samples.

The presence of sigma phase can be an indication that the thermodynamic databases are missing the exact formation temperature of the phase, and in this case, other criteria may help to guide the phase stabilities of the alloy. Tsai et al. [31], [32] proposed two criteria to guide the development of duplex HEAs while controlling the composition of the alloy to avoid the formation of sigma phase, which has detrimental mechanical properties. The first of Tsai's criteria is the Valence Electron Concentration (VEC), which corresponds to a weighted average of the valence electrons contributed by each element in the HEA. However, the ranges of VEC associated with sigma-phase formation and duplex (BCC + FCC) microstructures overlap significantly. This overlap limits the effectiveness of VEC alone in distinguishing whether a given alloy will develop a

duplex structure without sigma-phase formation. Tsai's second criterion, known as the Pair of Sigma-Forming Elements (PSFE), quantifies the propensity of element pairs within an alloy to form the sigma phase. By combining these two criteria, Tsai demonstrated a predictive framework for identifying compositions likely to form a duplex microstructure while minimizing the risk of sigma phase development. These criteria have proven effective in guiding the design of duplex HEAs across various systems [31],[32].

According to Tsai's criteria, alloys with VEC values between 6.88 and 7.84 and/or PSFE percentages exceeding 45% are prone to sigma phase formation. The VEC and PSFE of $Cr_{51.5}Co_{15}Ni_{33.5}$ alloy are, respectively, 7.79 and 66.7%, therefore this criterion seems to contradict the thermodynamic calculations, indicating that sigma phase would be formed on this alloy, as seen experimentally. It is worth to mention that this criterion has been proved useful in many literatures works, in some cases surpassing the predictability of CALPHAD calculations, especially on cases where the CALPHAD database was constructed without the full assessment of the binaries and ternaries of the constituting elements of the alloy [40]. Interestingly in this case, the full ternary is described in both databases but as evidenced in the previous section, the alloy is very close to sigma-prone compositions meaning that the CALPHAD calculations are probably missing the exact equilibrium by a small amount. The Thermo-Calc® software, similar to Pandat®, failed to predict the formation of the sigma phase for the alloy investigated in this study as shown in Figure 2.4.

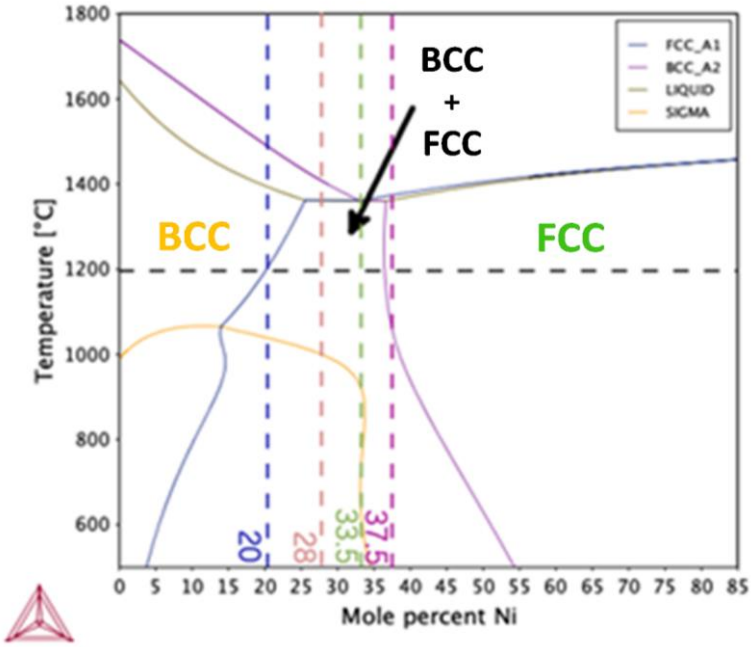

Figure 2.4: Isopleth of the CrCoNi ternary diagram calculated using the CALPHAD method and the TCHEA3 database, with the Co content fixed at 15%, showing the phase changes present for different compositions from 1800 °C down to low temperatures.

Therefore, we show here the usefulness of Tsai's criteria also in these more challenging situations, especially if combined with the predicting capability of CALPHAD calculations.

Given the importance of the CrCoNi system and problem displayed in the thermodynamic databases, a more in-depth study of this composition follows to guide future new database adjustments for this system.

2.3.3 OPTICAL AND SCANNING ELECTRON MICROSCOPY ANALYSIS.

The microstructural analysis of the material produced was first carried out using optical microscopy. From the diffraction analysis it was assumed the presence of both FCC and BCC phases and the possibility of sigma phase being present. From OM images, it can be noted that both samples present two distinct phases. As illustrated in figure 2.5 below, the as cast and homogenized material consist of two coexisting phases, and the morphology of these phases vary depending on the sample analyzed and the region of such sample. Images 2.5(a) and 2.5(b), referring to as-cast material, show that the two phases are arranged

differently depending on the region of the sample. In figure 2.5(a) the two phases present are organized in a eutectic morphology, while in figure 2.5(b) there is also the presence of dendritic regions of the matrix phase. Morphological variations are also evident in the homogenized sample. Figures 2.5(c) and (d), which depict different regions of the material reveal the presence of dendritic morphologies in certain areas of the material (Figure 2.5 (c)), while other regions still exhibit eutectic structures. This variation suggests localized differences in the solidification behavior prior to the homogenization process.

Based on the computational predictions from CALPHAD simulations, which indicated the coexistence of BCC and FCC phases, the darker phase seems to better match as the BCC phase and the other phase is identified as FCC because of their volumetric functions. As it will be shown in the next sessions this idea is further supported by EDS and electron diffraction patterns. Though CALPHAD seems to predict the correctly which phase is more abundant in the material, there is not a very good match of the exact predicted numbers for the fractions of each phase when comparing with experimental results. Considering the volumetric fraction calculations using OM data, there are notable differences between the predicted values for each phase. For homogenized sample, for example, the darker phase's volumetric fraction was 19,70% and the calculated BCC fraction with CALPHAD was 11.78%. All the values are listed in table 2.3.

Table 2.3: Different measures of volumetric fractions of the phases in the as cast and homogenized samples with the average error.

Sample	Average volumetric percentage of the dark phase	Average volumetric percentage of the clearer phase	Average error
As Cast	20.180	79.820	4.145
Homogenized	19.698	80.302	2.109

A possible explanation for the difference between the predicted phase fractions and the experimental fractions is that the sigma phase, that was latter detected by other techniques may exhibit shades of gray and contrast that may

look indicate those of the BCC phase, as will be displayed later. Sigma usually displays a morphological aspect that seems like big BCC lamellae. This was analyzed by SEM with BSE and EDS techniques and are exposed in the next sections.

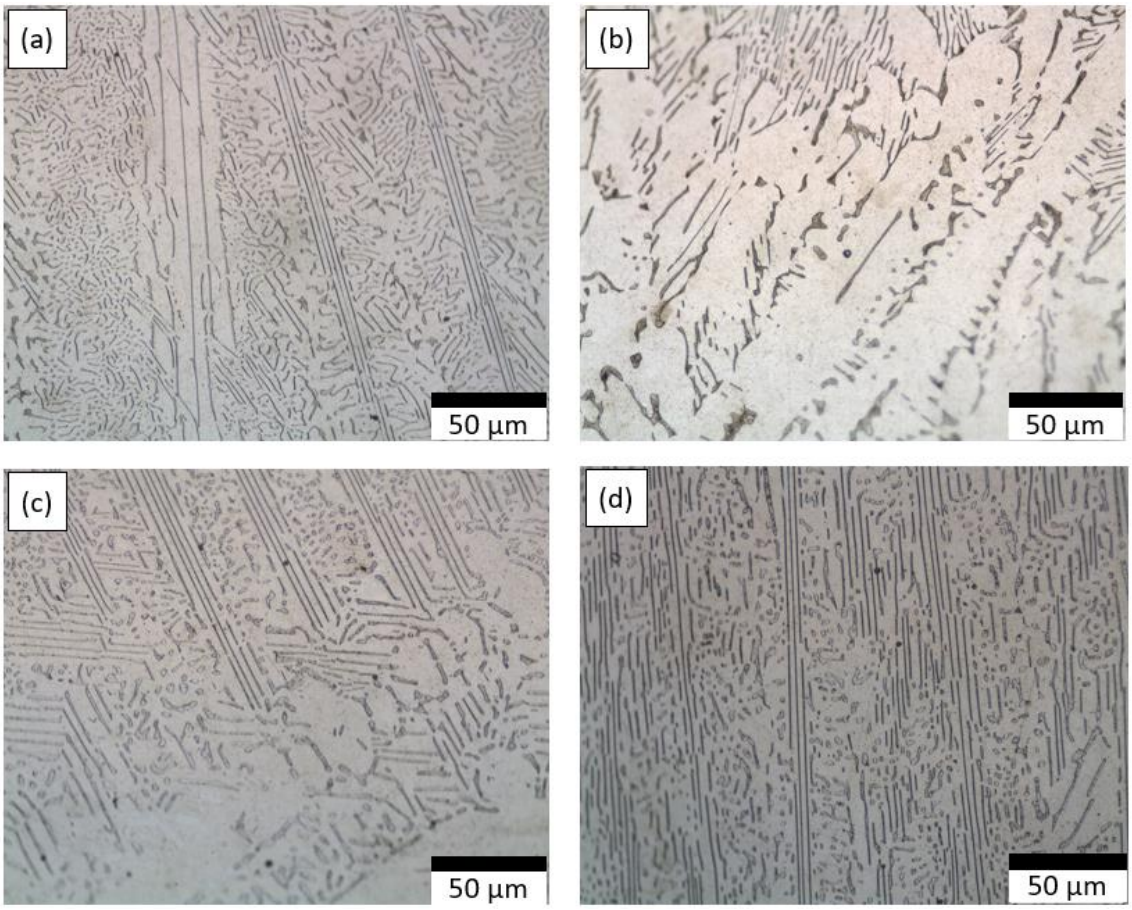

Figure 2.5: Optical microscopy images of samples as cast and homogenized. (a) and (b) refer to the as-cast, (c) and (d) to the homogenized samples, respectively.

The analysis via EDS confirmed the expected composition of the material: The measured atomic compositions of the samples were 51.1 at% Cr, 15.0 at% Co, and 33.8 at% Ni for as-cast sample, and 51.3 at% Cr, 15.0 at% Co, and 33.7 at% Ni homogenized material. Figure 2.6 shows SEM analysis on the homogenized sample. Figure 2.6(a) shows a BSE image that displays three main different phases based on the contrast of the image. EDS composition analyses were performed in each one of the three phases as indicated by the arrows in the image and the results can be seen in table 2.4.

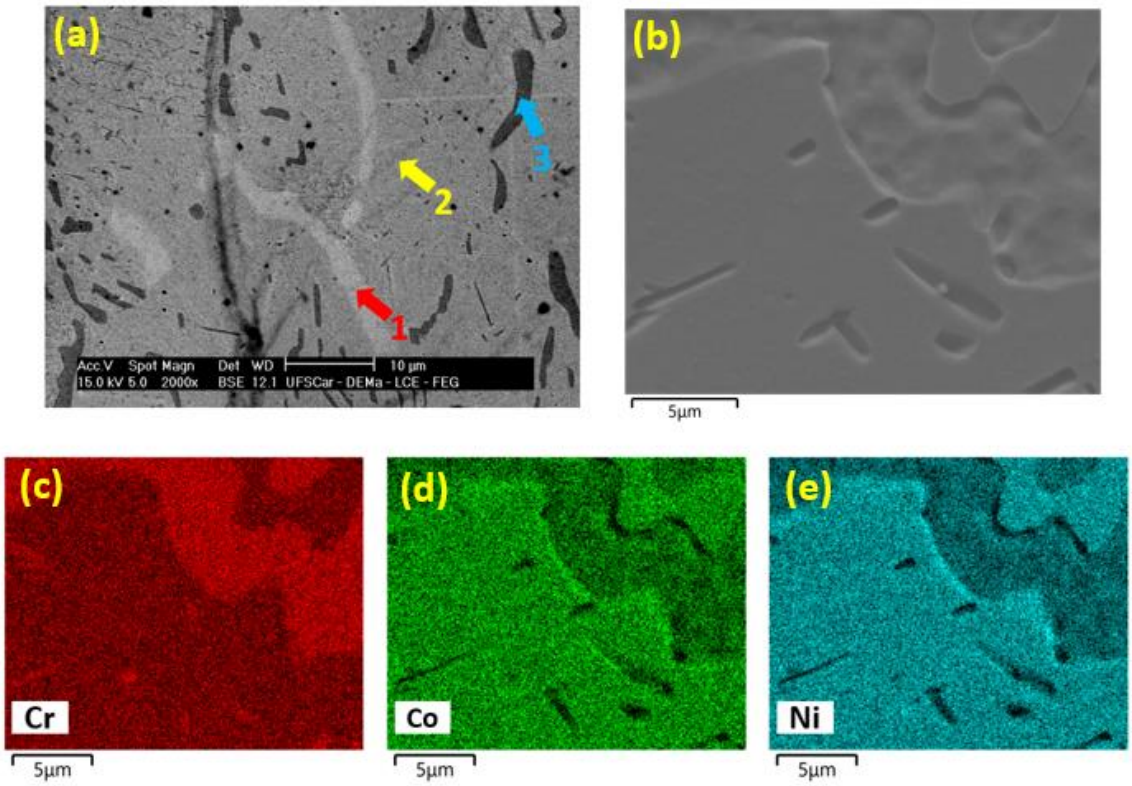

Figure 2.6: (a) and (b): BSE and SE images of homogenized sample. (c), (d) and (e) present compositional maps of the same sample.

The results shown in table 2.4 suggest that regions 1, 2 and 3 shown in figure 2.6(a) when put aside the theoretical compositions correspond respectively to sigma, FCC, and BCC phases It is interesting to note that while such phases appear clearly different when observed via BSE imaging, in OM and Se images, the difference between BCC and sigma phases seems to be less significant. It is interesting to note that although different, there is a similarity in composition between the sigma and BCC phases.

Table 2.4: EDS composition measured for the regions 1, 2 and 3 shown in figure 2.6 (a). It's clear that region 1 seems to be sigma phase as well as regions 2 and three have compositions very similar to FCC and BCC phases, respectively.

Region	at% Cr	at% Co	at% Ni
1 – Sigma	64.4	14.1	21.5
2 – FCC	48.8	15.4	35.8
3 - BCC	76.6	9.8	13.6

As a result, when analyzing element maps such as those in Figures 2.6(b), (c), and (d), it appears that, although different morphologies can be observed in some regions of the sample, like in Figure 2.6(a) it can be difficult to determine whether they correspond to sigma or BCC phases based solely on morphology or even on EDS mapping. This is because, while EDS effectively distinguishes the matrix from other phases, it is not as effective in differentiating between sigma and BCC phases due to their similarity in composition. Given this difficulty, it will be shown next that observations of the sigma phase become much more straightforward on etched samples, which are validated by a combination of EDS and/or alternative characterization techniques, such as EBSD.

Figures 2.7(a) and 2.7(b) present the distinct morphologies observed in Homogenized sample and illustrate variations in chemical contrast and surface topography depending on the analyzed phase. The phase presumed to be BCC appears darker in the backscattered electron (BSE) images, suggesting a lower atomic number contrast (Z-contrast) or a higher concentration of light elements compared to the phase identified as FCC. This observation is consistent with the compositional data presented in Table 2.2, as the BCC phase is expected to be enriched in Cr, whereas the FCC phase contains higher concentrations of Ni and Co, elements with higher atomic numbers. These findings are in good agreement with the phase compositions predicted by CALPHAD calculations for Co, Cr and Ni.

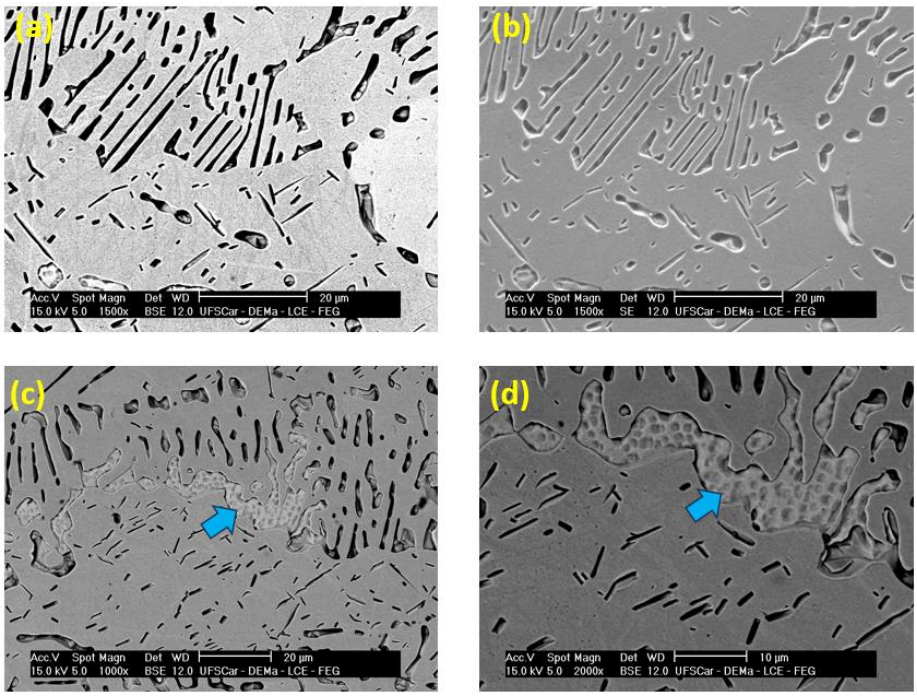

Figure 2.7: BSE (a) and SE (b) images showing details of the morphologies of the second phase in the homogenized material. (c) and (d) present different magnifications of regions of that sample in which the second phase has chemical composition close to the one expected for sigma phase.

By performing point EDS analyses on different morphologies of the second phase, it can be shown that the highlighted region in Figure 2.7(c) and (d) corresponds to the sigma phase. The average composition of this gray phase, as indicated in the figure, falls within a range of 61–64 at% Cr, 16–17 at% Co, and 19–21 at% Ni, suggesting that this microconstituent is very likely the sigma phase. By the image, the etching is very different in the sigma and bcc phases, however it can also be seen that the morphologies are very similar, which would make the identification of sigma and BCC phases much more challenging without it.

To gain a deeper understanding of the microstructural characteristics in terms of crystallographic features, Electron Backscatter Diffraction (EBSD) analysis was conducted. The results confirmed that the three distinct morphologies identified in homogenized sample correspond to different phases. As illustrated in Figure 2.8, the EBSD phase map delineates these constituents:

the matrix phase (FCC) shown in red, the BCC phase in yellow, and the sigma phase in green. The micrograph reveals that the sigma phase exhibits only subtle morphological differences relative to the BCC phase, which accounts for the occasional ambiguity observed in EDS measurements of the lamellar regions—sometimes indicating a BCC composition and, in other instances, a sigma composition. This morphological similarity complicates the unambiguous differentiation between the two phases in the absence of complementary EBSD analysis or selective chemical etching.

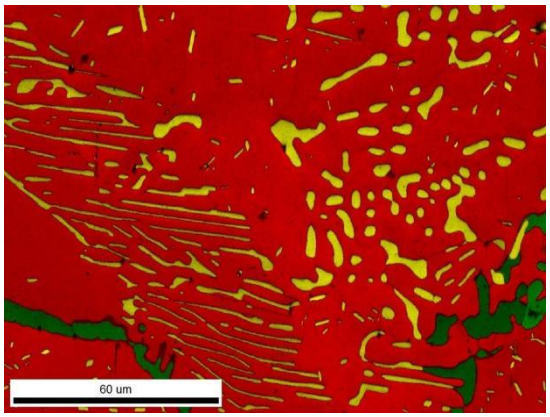

Figure 2.8: EBSD phase mapping of homogenized sample. it is possible to note that besides the matrix FCC face (red), BCC (yellow) and sigma (green) can be seen.

The presence of the sigma phase also accounts for discrepancies between the calculated volumetric fractions of FCC and BCC phases and those obtained from optical microscopy. The calculated phase fractions indicate 80.3% FCC and 19.7% BCC, whereas the predicted values were approximately 88% FCC and 12% BCC. This discrepancy arises because the presence of the sigma phase increases the apparent fraction of BCC when observed via optical microscopy due to the morphological similarity between the two phases and their tonality. Consequently, the total observed FCC fraction is reduced, as part of the microstructure that appears to be BCC includes sigma phase.

2.3.4 TRANSMISSION ELECTRON MICROSCOPY

Several fine features are observed in the homogenized sample presented previously, to go further in the investigation of structural characteristics and chemical composition of individual phases and observe the finer components of the microstructure, Transmission Electron Microscopy (TEM) was employed. This technique was applied homogenized material, from which STEM Bright Field (BF) and Dark Field (DF) images were captured and are presented in Figure 2.9.

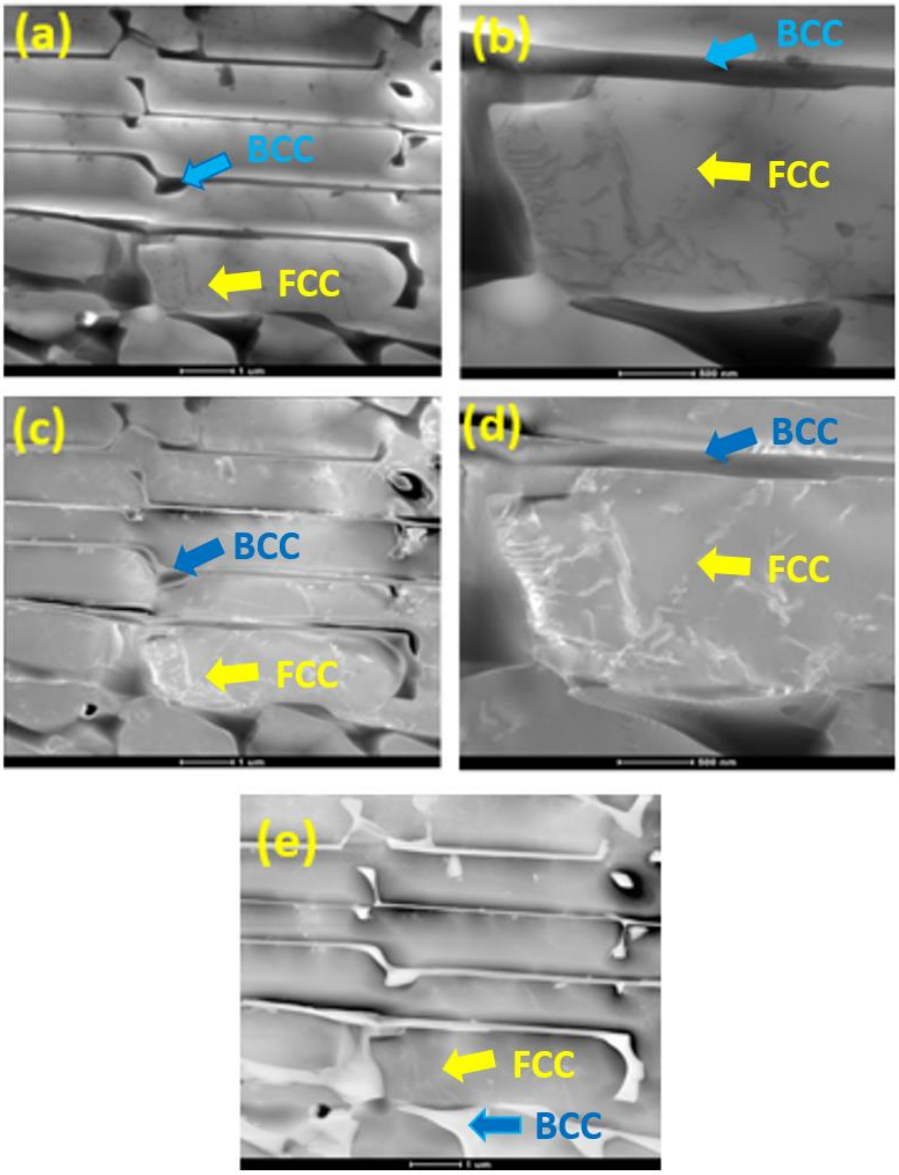

Figure 2.9: STEM Bright Field (A, B), Dark Field (C, D), and HAADF (E) images of homogenized sample. Contrast variations in (E) are attributed to artifacts from

the TEM electropolishing process, causing differential Thickness between phases.

These images reveal two phases, presumably FCC being the more abundant and BCC the other phase, with apparent dislocations within the FCC matrix. This interpretation is supported by subsequent EDS analysis that determined the chemical composition of each phase. The overall composition of phases is consistent with values previously observed by SEM. The EDS mappings displayed in Figure 2.10 (e), (f) and (g) shows a similar trend where the FCC phase is richer in Ni and what was assumed to be a BCC phase is richer in Cr. The composition of each phase is detailed in Figure 2.10, which aligns with previous results. Regions labeled (a) and (b) correspond to areas used for making these compositional measurements listed in the figure.

The EDS data obtained from SEM (Table 2.3) and TEM (Figure 2.10) indicate that the atomic composition of the FCC phase in homogenized sample is very similar in both analyses. However, the BCC phase composition measured by TEM shows a slight difference compared to SEM, with a higher Cr content. This discrepancy could be linked to the possible small size or thickness of the BCC phase. If the phase whose composition is been measured is not thick enough, then EDS analysis performed in SEM microscope can lead to imprecise values for the percentage of elements when compared to EDS taken by TEM if the constituent where EDS is being applied is very thin. That happens because the samples used in SEM are much thicker than the ones used in TEM. For that reason, the signal collected by EDS detectors to quantify the elements in the material can detect not only signal generated by the constituent of interest (The BCC phase for example) but also signal detected by other phases or particles altering the quantitative result of the analysis. That can make it challenging to accurately determine its composition using SEM in some cases, as the interaction volume may include contributions from surrounding phases. In TEM, as the sample is much thinner, the signal received from parts of the material others than that of interest is minimized, and the composition obtained by EDS tends to be more precise. Nevertheless, as both measures are relatively close to each other,

the difference between then can also be related to the errors relative to the measures in EDS in SEM and TEM as well as composition fluctuations within the sample.

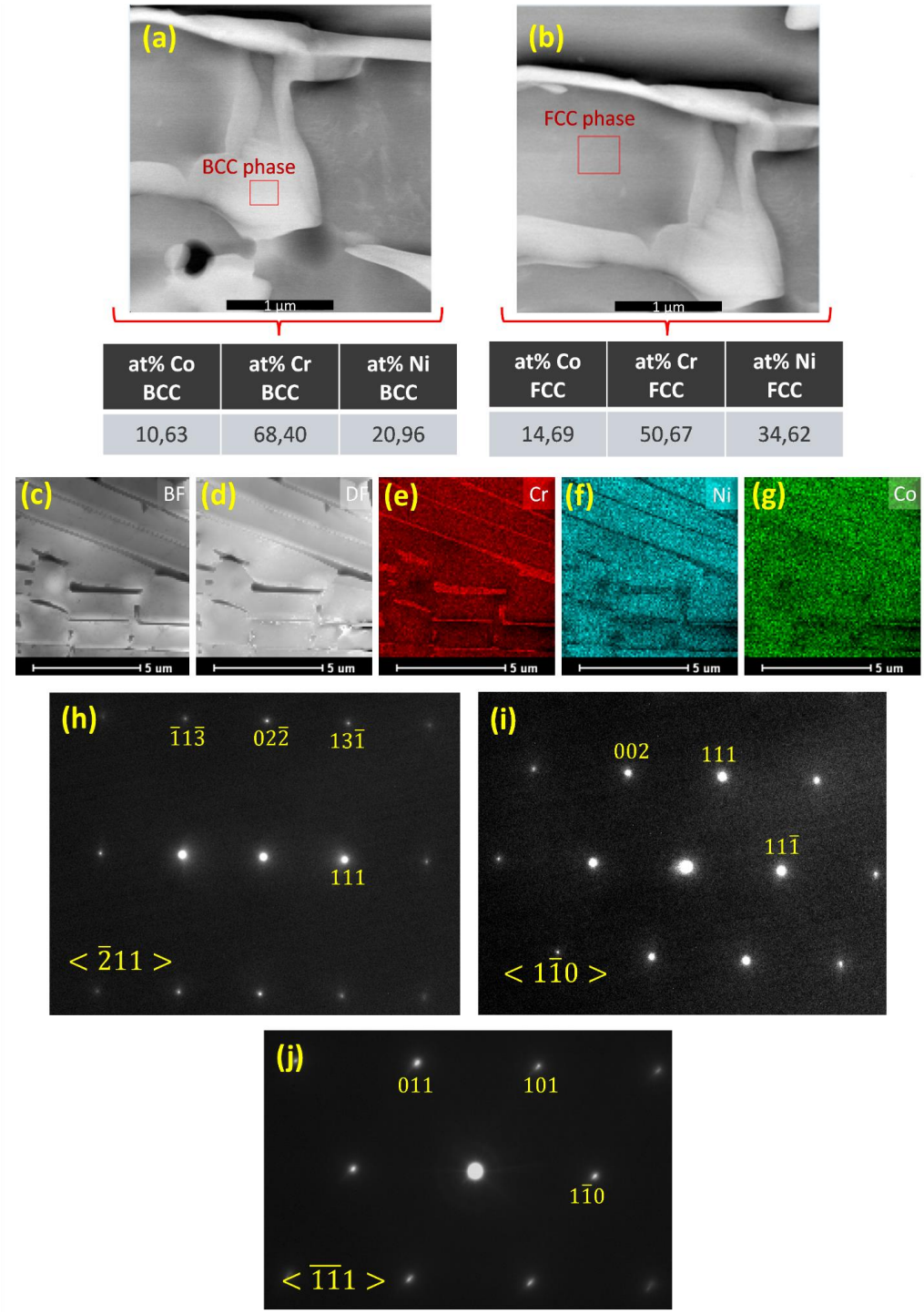

Figure 2.10: (a) and (b) EDS data collected for BCC and FCC phases, respectively. (c) show STEM BF image of region containing FCC and BCC phases in the alloy. (d) show the same region, now in a STEM – DF image. (e),

(f) and (g) show Cr, Ni and Co composition measurements for FCC and BCC phases, (h), (i) show electron diffraction patterns of FCC phase and (j) shows electron diffraction pattern for BCC phase.

Electron diffraction patterns were also collected to confirm the structure of each phase. Electron diffraction patterns were taken for each phase, as seen in Figure 2.10 (h), (i), and (j). The results confirm that the matrix indeed consists primarily of an FCC phase with the smaller, Cr-rich, BCC phase.

While FCC and BCC phases could be characterized by TEM, sigma could not be found in the samples. This could be due to the heterogenous dispersion of this phase in the matrix as seen previously or due to the electropolishing attacking preferentially the sigma phase. This last possibility is more likely since different parameters were used to prepare samples and in none of these analyses' sigma was found.

2.3.5 NANOINTENTATION ANALYSIS

Although the material did not have the intended microstructure, a study to evaluate how promising a duplex CrCoNi microstructure can still be performed via nanoindentation tests. These tests were performed in the specimen to evaluate the mechanical properties of the non-deleterious phases, FCC, and BCC.

In addition to measuring the hardness of each phase, the nanoindentation tests also allowed for the determination of the elastic modulus, as well as the estimation of the hardening coefficient and the yield stress using previously presented models. The hardness and elastic modulus of each phase are shown in the violin diagrams in Figure 2.11 (a) and (b), respectively.

To calculate the elastic modulus, both phases were assumed to have a Poisson's ratio of 0.3 [36]. As expected, the BCC phase exhibited higher hardness than the FCC phase. While the average hardness of the FCC matrix was 3308 MPa, the BCC phase had an overall hardness of 4161 MPa. This indicates that as initially predicted, the BCC phase is indeed a stronger phase that could act as a reinforcement for the FCC phase. Regarding the elastic

modulus, the FCC phase showed a slightly higher overall value compared to the BCC phase.

Figure 2.11 (c) presents a violin diagram displaying the strain hardening coefficient for each phase. By using the equation proposed by Bertoli et al. [35] to estimate the SFE in CrCoNi alloys together with the composition of the FCC phase reported in Figure 2.10, a SFE of 9 mJ/m^2 can be estimated for the FCC matrix, which would indicate that the matrix is prone to exhibit TRIP effect [35]. Given that the FCC matrix has a low stacking-fault energy (SFE), cross-slip of dislocations is more difficult, leading to a higher hardening coefficient (0.31) compared to the BCC phase (0.21).

In Figure 11 (d), the violin diagram shows the estimated yield stress for each phase. The values for the FCC phase are well-concentrated around an average of 410 MPa, whereas the BCC phase exhibits a broader distribution, with an overall average of 1077 MPa. The broader distribution of the predicted values of the BCC phase is most likely due to subsurface effects of the FCC phase on smaller particles of the second phase. It is important to highlight that the latter value is likely overestimated due to modeling limitations, as values are widely spread between 280 MPa and 1650 MPa. Despite this, the overall yield stress of the BCC phase remains higher than that of the FCC phase, which is expected due to the greater ease of dislocation movement in the latter.

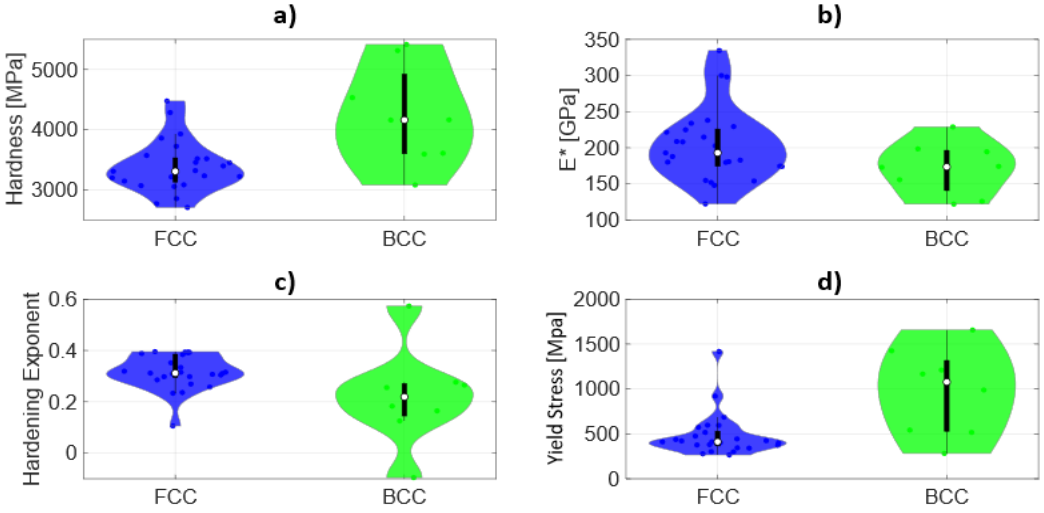

Figure 2.11: violin diagrams presenting (a) the nano hardness; (b) elastic modulus; (c) estimation of the strain hardening coefficient and (d) estimations for the yield stress distributions for matrix (FCC) and bcc phases.

Although the alloy did not exhibit a fully duplex microstructure consisting solely of FCC and BCC phases, the nanoindentation results suggest that regions where the duplex structure is present exhibit promising mechanical characteristics. The FCC matrix phase, characterized by its lower hardness, low stacking-fault energy (SFE) and higher strain hardening exponent (when compared to BCC), all characteristics of a very tough material, is complemented by the presence of harder and mechanically stronger BCC phases. This combination suggests that an optimized duplex CrCoNi alloy, without sigma, could achieve a desirable balance between strength and ductility. Therefore, further studies exploring optimized compositional ranges, informed by the results of this work, would be of great interest for the development of true duplex CrCoNi alloys with tailored mechanical properties.

2.4 CONCLUSIONS

A CrCoNi-based duplex multiprincipal element alloy (HEA) with the composition $Cr_{51.5}Co_{15}Ni_{33.5}$ was designed and produced based on CALPHAD predictions. The microstructural and mechanical properties of the alloy were characterized using SEM, TEM, XRD, synchrotron diffraction, and nanoindentation testing. The designed alloy exhibited both FCC and BCC phases in the as-cast condition, however, sigma phase formed after homogenization, contradicting the CALPHAD simulations but aligning with Tsai's criteria, which successfully anticipated its formation.

The sigma phase was dispersed throughout the microstructure and morphologically similar to the BCC phase, making its detection challenging without EBSD and chemical etching. Nanoindentation testing confirmed that the FCC matrix exhibited high ductility and a high strain hardening coefficient, key indicators of superior fracture toughness. The BCC phase showed higher hardness and predicted yield strength, reinforcing the potential of duplex microstructures in enhancing strength while maintaining ductility.

It was also shown that thermodynamic approach presented by CALPHAD method was not in accordance with TSAI´s criteria´s predictions. It shows that

improvement of thermodynamic databases regarding HEAs are still required to simulate phase stability and microstructural characteristics of these alloys.

CHAPTER 3 – EXPLORING INTERFACIAL ENERGY MODELLING FOR $L1_2$ PRECIPITATION HARDENED HEAS

3.1 INTRODUCTION

High-entropy alloys (HEAs), also referred to as multicomponent alloys, constitute a class of metallic materials conceived without a single dominant element accompanied by minor additions, but rather composed of multiple principal elements in near-equiatomic proportions [41]. Interest in these alloys arises from the exceptional properties they may exhibit, such as outstanding toughness and high mechanical strength at cryogenic temperatures. In addition, increasing attention has been devoted to multicomponent alloys suitable for high-temperature applications, which has led to the emergence of a new subclass known as high-entropy superalloys (HESAs) [42].

The development of HESAs is motivated by the prospect of partially replacing or complementing conventional Ni-based superalloys, which are traditionally employed in applications requiring high-temperature mechanical strength. In this context, it is also reasonable to draw parallels between Ni-based superalloys and HEAs, since several conventional superalloys may be classified as high-entropy alloys based on their compositional complexity. Nickel-based superalloys are specifically engineered to operate at elevated temperatures while retaining their mechanical integrity. Alloys such as INCONEL 625, for instance, can be employed in environments where temperatures exceed 1100 °C [43].

The development of Ni-based superalloys began in the 1950s and 1960s, driven primarily by the aerospace industry, which demanded materials capable of withstanding progressively higher operating temperatures to satisfy the stringent performance requirements of aircraft engines and turbine components [44].

The mechanical strength and thermal stability exhibited by these materials are generally associated with specific microstructural features, which typically consist of an FCC matrix containing a dispersion of precipitates. Among these precipitates, the γ′ and γ″ phases play a particularly important role. Precipitate characteristics, such as volume fraction and average size, strongly influence the

mechanical properties of the alloy, as they directly affect the mechanisms governing dislocation motion within the superalloy, resulting in a favorable combination of properties. In addition to enhancing mechanical strength, the presence of precipitates also contributes significantly to the thermal stability of these alloys [45].

In this context, the investigation of precipitation processes in Ni-based superalloys, as well as in HEAs that rely on similar strengthening mechanisms, is essential for advancing modern superalloy design. Studies on the thermal stability and mechanical behavior of conventional Ni-based superalloys are particularly relevant for understanding analogous phenomena in high-entropy superalloys. Thermodynamic and kinetic simulation approaches, such as those enabled by the CALPHAD (Calculation of Phase Diagrams) method, constitute powerful tools for predicting phase stability and identifying promising compositions for further investigation [46].

One of the key parameters governing precipitation behavior in both Ni-based and high-entropy superalloys is the interfacial energy between the matrix and the precipitates [47]. Interfacial energy directly influences precipitate size, morphology, and stability. As discussed in the following sections, its accurate determination plays a critical role in the reliability of precipitation simulations and in achieving consistency with experimental observations.

Consequently, the development and application of methods capable of predicting and determining interfacial energies between phases in a given material are essential for supplying reliable input to thermodynamic and kinetic simulation models, thereby enabling more accurate and physically meaningful results. Experimental measurement of interfacial energies between phases in metallic alloys is notoriously challenging. Among the alternative approaches available for estimating interfacial energies, first-principles computational methods stand out, particularly those based on Density Functional Theory (DFT). DFT is widely recognized for its ability to predict a broad range of material properties with reasonable accuracy, especially fundamental properties related to electronic structure and atomic bonding, as well as structural properties such as elastic constants. Moreover, the DFT framework is well suited for addressing

problems involving surfaces and interfaces at the atomic scale, making it a valuable tool for the investigation of interfacial phenomena in complex alloys.

In the present work, the primary objective is to evaluate the effectiveness of estimating interfacial energies of γ′ and γ″ precipitates embedded in the γ matrix of Ni-based superalloys using Density Functional Theory (DFT). To this end, a high-entropy alloy with the atomic composition $Ni_{57.5}Fe_{20.0}Cr_{12.5}Ni_{2.5}Ti_{5.0}Al_{2.5}$ was produced and experimentally characterized to obtain precipitation-related data. The selection of this HEA was based on high-throughput thermodynamic calculations performed using Pandat®. CALPHAD simulations indicated that this alloy is a promising candidate for applications analogous to those of conventional Ni-based superalloys.

The choice of each alloying element reflects its contribution to the targeted properties. Nickel stabilizes the FCC matrix and provides thermal stability at elevated temperatures. Chromium promotes corrosion resistance through the formation of passive films, while titanium and aluminum favor the formation of $L1_2$-ordered precipitates within the matrix. Iron was selected as a cost-effective substitute for cobalt, which is commonly used in similar alloys but is significantly more expensive. The addition of niobium aims to further enhance the tendency for the formation of strong $L1_2$ precipitates, as this element is known to stabilize this phase and increase precipitate strength.

The alloy investigated in this study had been previously examined by our research group. Microstructural analyses using SEM and TEM, combined with mechanical testing, demonstrated that the alloy exhibits an excellent balance of mechanical properties. This behavior is attributed to the combined effects of solid-solution strengthening and precipitation strengthening associated with the presence of $L1_2$ precipitates.

The second objective of this work is to incorporate the interfacial energy values obtained from DFT calculations into precipitation models within the CALPHAD framework using Pandat® software, and to compare the simulation results with experimental data to assess their accuracy. This approach enables verification of the suitability of DFT for calculating interfacial energies in the studied alloys and provides a basis for proposing the calculation of additional

thermodynamic and kinetic parameters. Ultimately, this methodology is intended to be extended to the investigation of high-entropy superalloys.

3.2 LITERATURE REVIEW

The use of metallic alloys in engineering and across different sectors of society is fundamentally governed by their material properties. Among the most relevant characteristics within an application context are mechanical strength, as exemplified by structural steels used in construction [48], and corrosion resistance, as observed in stainless steels [49].

With technological advancements in aircraft, engines, and turbine systems, it has become increasingly critical for engineering components to operate at the highest possible temperatures to improve efficiency [45], while avoiding severe degradation of their properties. These requirements are commonly encompassed by the term *thermal stability*, which refers to the stability of phases and microstructural constituents over a temperature range extending beyond that typically tolerated by conventional metallic materials.

3.2.1 SUPERALLOYS

The most prominent examples of metallic materials exhibiting high-temperature thermal stability are superalloys [50,51], particularly Ni-based superalloys. The designation “super” derives precisely from their exceptional ability to operate safely at temperatures where other metallic alloys would suffer from deleterious effects such as phase transformations, creep, oxidation, and corrosion [52,53].

The application of this class of alloys in aerospace components becomes evident when considering the schematic of a turbine such as the Rolls-Royce Trent 800 (Figure 3.1) [52]. This illustration highlights the wide variety of materials required to ensure the proper operation of such engines. In addition to thermal stability, components located in the turbine hot section must withstand aggressive phenomena such as oxidation and corrosion [51,53], which are particularly severe at elevated temperatures. Consequently, the combination of these demanding requirements has driven the development of materials exhibiting an

outstanding balance of thermal stability, mechanical strength, and corrosion resistance.

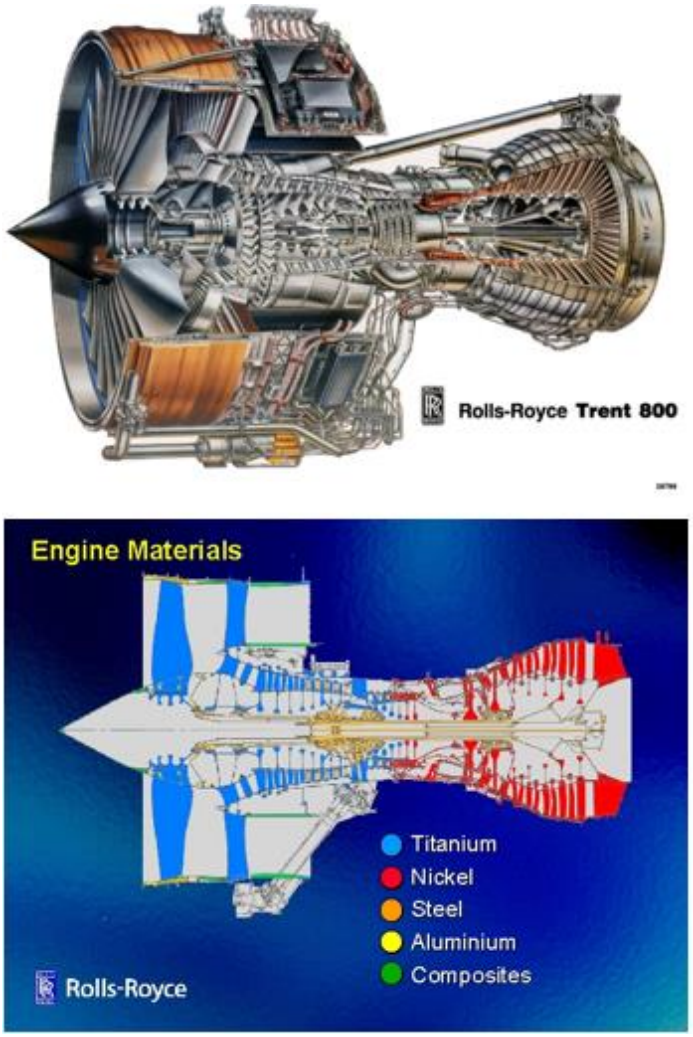

Figure 3.1: Schematic diagram showing different materials used in bypass-type turbines, characteristic of jet aircraft. Note the use of Ni in the turbine's hot sections [54, 55].

Other applications of superalloys include nuclear reactors and submarines, the petroleum industry, heat exchangers, and structural components requiring high corrosion resistance, typically found in the chemical industry [56].

3.2.2 EXTENDING SUPERALLOY FEATURES TO HEAs

More recently, the superalloy concept has been extended to high-entropy alloys, giving rise to the class known as High-Entropy Superalloys (HESAs). At

first glance, this concept appears to contradict the original philosophy of high-entropy alloys, which initially emphasized compositions exhibiting wide single-phase stability ranges and simple crystal structures, such as FCC, BCC, and HCP. However, as research on HEAs has progressed, the presence of secondary phases has increasingly been recognized as potentially beneficial, leading to alloy designs that combine solid-solution matrices with ordered phases, such as $L1_2$. This type of microstructural configuration closely resembles that found in conventional Ni-based superalloys and is a key factor underlying their exceptional properties.

The integration of HEA and superalloy concepts provides the opportunity to achieve a favorable balance between mechanical performance and production cost, which can be partially attributed to the increased use of relatively inexpensive elements such as iron [52,89], as illustrated in Figure 3.2. In addition, HESAs may exhibit lower density compared to traditional Ni-based superalloys due to their higher titanium content [57]. Furthermore, the vast compositional space inherent to multicomponent alloys, together with the possibility of exploiting additional strengthening mechanisms—such as short-range ordering [52,58]—helps to explain the growing interest in HESAs as potential alternatives to replace or complement conventional superalloys.

It is also important to note that the mechanisms responsible for the properties of HESAs are largely analogous to those governing conventional superalloys. In particular, the combination of a matrix and coherent precipitates, such as FCC and $L1_2$ phases, enables the physical metallurgy of HESAs to be investigated using the well-established metallurgical framework developed for Ni-based superalloys as a guiding reference.

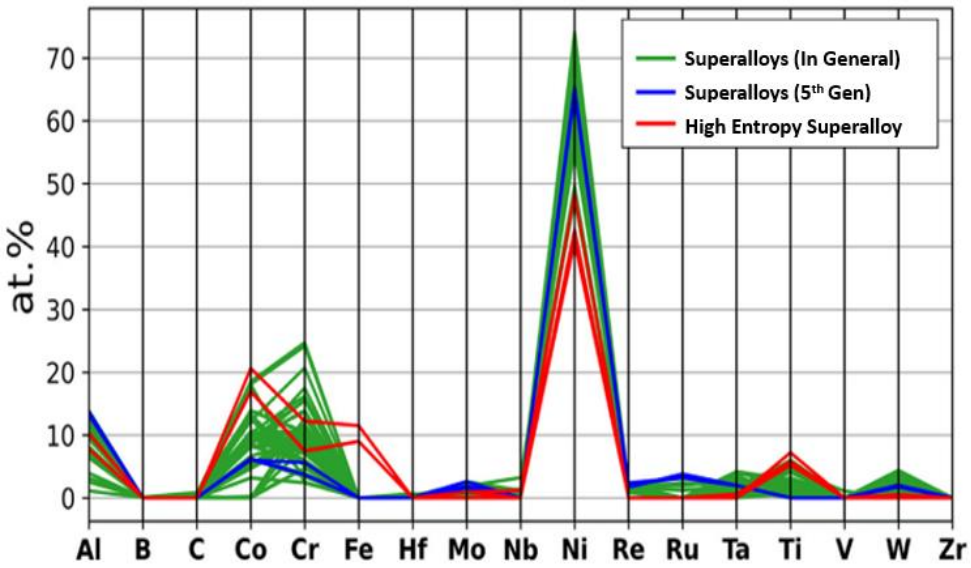

Figure 3.2: Comparison of the percentages of elements typically used in different types of superalloys. It is noted that superalloys in general, the so-called 5th generation of superalloys, and high-entropy superalloys tend to have nickel as their major element. Adapted from [57].

3.2.3 PHYSICAL METALLURGY OF SUPERALLOYS

Superalloys, similarly, to other metallic alloys such as steels, rely on multiple strengthening mechanisms that operate simultaneously to enhance mechanical performance. The overall mechanical strength of these alloys results from the combined contributions of solid-solution strengthening, the intrinsic strength of the crystal lattice, and, most importantly in high-strength compositions, precipitation strengthening. The effectiveness of precipitates in increasing mechanical strength arises from their ability to impede the motion of dislocations within the material.

From a mechanical standpoint, when dislocations—linear defects that move along atomic planes in the crystal structure [59]—interact with precipitates, their propagation is hindered. The nature of this interaction is primarily governed by precipitate size and by the average spacing between precipitates. Fine precipitates are typically sheared by moving dislocations (Figure 3.3), whereas larger precipitates are bypassed through the Orowan looping mechanism [60].

The former interaction generally leads to a more pronounced contribution to the mechanical strength of the alloy.

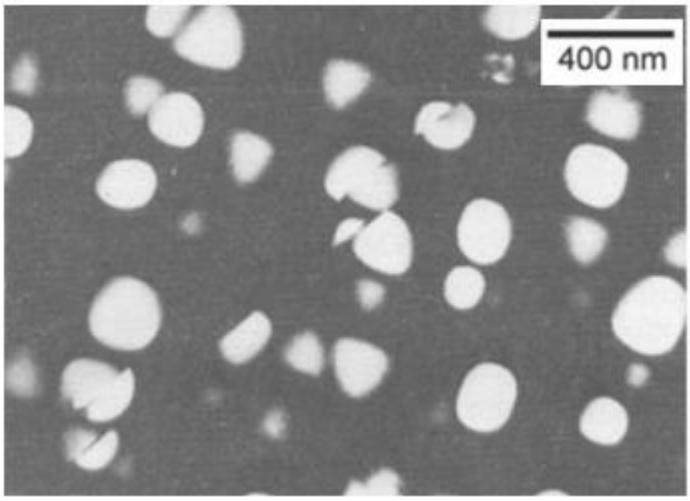

Figure 3.3: Dark-field transmission electron microscopy (TEM) image showing $L1_2$-type precipitates being sheared by dislocations in a Nimonic 105 Ni-superalloy [54].

In order to shear precipitates, dislocations in Ni-based superalloys must move in pairs [95], forming configurations known as superdislocations, as illustrated in Figure 3.4. This behavior arises because $L1_2$ precipitates contain different atomic species at the corner and face-centered positions of the unit cell, which leads to a mismatch between the Burgers vector of the precipitate and that of the surrounding matrix. Specifically, although both phases share close-packed {111} planes, the magnitude of the Burgers vector in the precipitate is twice that of the matrix.

As a result, for a dislocation to traverse a precipitate, a crystallographic defect must be created within it, known as an antiphase boundary (APB). The energy associated with this defect is referred to as the antiphase boundary energy (APBE), which depends on both the composition [61] and the size of the precipitate [60]. The paired motion of dislocations ensures that the combined Burgers vectors restore the ordered crystal structure of the precipitate to its original state following the passage of the second dislocation.

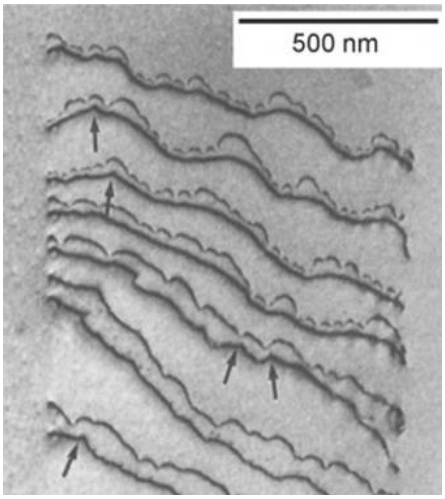

Figure 3.4: transmission electron microscopy (TEM) image showing pairs of dislocations in the Nimonic PE16 alloy [54].

To shear precipitates, dislocations in Ni-based superalloys must move in pairs [95], forming configurations known as superdislocations, as shown in Figure 3.4. This behavior arises because $L1_2$ precipitates contain different atomic species at the corner and face-centered positions of the unit cell, which causes a mismatch between the Burgers vector of the precipitate and that of the surrounding matrix. Specifically, although both phases share close-packed {111} planes, the magnitude of the Burgers vector in the precipitate is twice that of the matrix.

Consequently, for a dislocation to pass through a precipitate, a crystallographic defect must be generated within it, known as an antiphase boundary (APB). The energy associated with this defect, referred to as the antiphase boundary energy (APBE), depends on the precipitate composition [61] as well as its size [60]. The paired motion of dislocations ensures that the combined Burgers vectors restore the ordered crystal structure of the precipitate to its original configuration after the passage of the second dislocation.

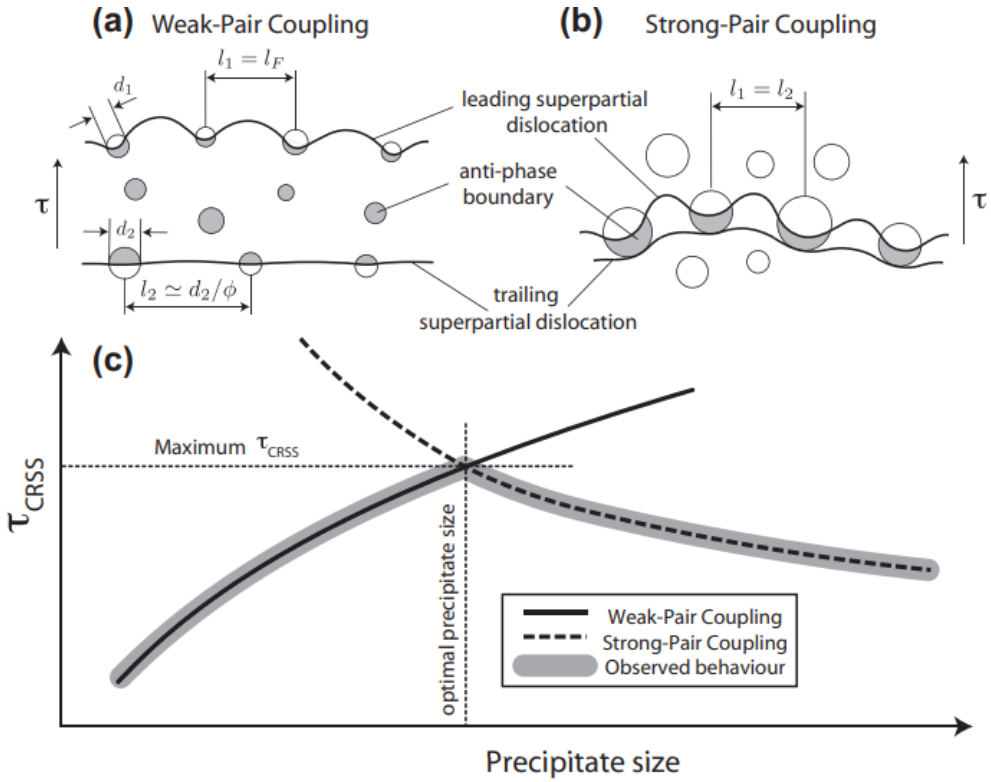

Figure 3.5: A schematic diagram describing the variation of resolved critical shear stress as a function of precipitate size. The diagram shows the cases of strong and weak coupling of superpartial pairs in relation to the anti-phase boundary and as a function of precipitate size. Adapted from [62].

The second scenario occurs when precipitates exceed a critical size, allowing the dislocation pair to interact with them in such a way that both dislocations can penetrate the precipitate simultaneously. In this case, the dislocation pair is referred to as a strongly coupled pair [63], and the strengthening contribution from precipitation begins to decrease as precipitates continue to grow [63]. Consequently, there exists an optimal spacing between the dislocations for which the resistance to dislocation motion is maximized. If the spacing between the dislocations is too large, the second dislocation penetrates the precipitate only after the first has completely traversed it. Conversely, if the dislocations are too closely spaced, the strengthening effect is reduced because the resulting antiphase boundary is small [44]. Therefore, neither extreme condition leads to a maximum improvement in mechanical properties, and an

intermediate dislocation spacing maximizes the contribution of precipitates to alloy strengthening. This optimal spacing is approximately comparable to the size of the precipitates that the dislocation pair must shear.

With respect to the factors governing thermal stability and creep resistance in these materials, the behavior of both the matrix and the precipitates must be considered. A key characteristic of the Ni-based superalloy matrix is that nickel does not undergo phase transformations when heated to very high temperatures, thereby ensuring the retention of the FCC crystal structure. The precipitates themselves also exhibit high thermal stability, maintaining their ordered structure at temperatures as high as approximately 1000 °C [64]. This stability allows strengthening mechanisms associated with antiphase boundary energy to remain active at elevated temperatures. In addition, carbides and borides play a significant role in enhancing creep resistance by impeding grain boundary motion at high temperatures, effectively acting as pinning sites for these interfaces [64]. In more extreme operating conditions, such as those encountered in turbine blades, creep deformation can be so severe that grain boundaries must be eliminated altogether through the use of single-crystal superalloys [52].

Another important aspect influencing superalloy properties is the lattice misfit between the matrix and the precipitates. Precipitates exhibiting a larger misfit relative to the matrix generate elastic stress fields that hinder dislocation motion and contribute to strengthening mechanisms associated with antiphase boundaries. In contrast, precipitates with a smaller misfit—that is, greater coherency with the matrix—tend to promote enhanced thermal stability. This behavior is related to the fact that increasing misfit substantially raises the system’s energy, primarily through an increase in interfacial energy, which acts as a driving force for precipitate instability or phase transformation [65].

It should be noted, however, that a trade-off exists between conventional mechanical strength and creep resistance (thermal stability) in superalloys. This balance is closely linked to the presence of antiphase boundaries and to the precipitation kinetics of the constituent phases, which influence precipitate morphology and size. Accordingly, an optimal compromise between these competing properties must be achieved. Since lattice misfit is strongly dependent

on precipitate composition, this consideration underscores the critical importance of appropriate alloy design and compositional selection.

3.2.4 ABOUT THE MAIN TYPES OF PRECIPITATES IN SUPERALLOYS

Typically, the most widely used superalloys—namely Ni-based superalloys—exhibit matrices with a predominantly disordered face-centered cubic (FCC) structure (space group $Fm\bar{3}m$) [66]. As is well established, this crystallographic structure is characteristic of metallic alloys in which the solvent element adopts an FCC lattice, which in this case is nickel. In the context of superalloys, the phase corresponding to this FCC matrix is commonly referred to as the gamma phase (γ), or simply gamma (γ).

Within this FCC matrix, several types of precipitates may form, each characterized by distinct crystal structures and chemical compositions. Among these, the most prominent are:

γ′ phase (gamma prime): This is the most prevalent and technologically important precipitate in Ni-based superalloys. γ′ precipitates are of the Ni_3X type, where X represents an alloying element other than Ni. The γ′ phase crystallizes in the $Pm\bar{3}m$ space group and adopts the ordered $L1_2$ structure, which is the designation by which this phase is commonly known. The orientation relationship between the γ′ precipitates and the FCC γ matrix is described by the following crystallographic relations:

$$\{010\}_{\gamma} \,//\, \{010\}_{\gamma'}$$
$$\langle 001\rangle_{\gamma} \,//\, \langle 001\rangle_{\gamma'}$$

An example of a γ′ precipitate unit cell, in which X corresponds to aluminum, is shown in Figure 3.6. This structure exhibits a strong similarity to the conventional FCC crystal lattice; however, in the case of the γ′ precipitate, nickel atoms occupy exclusively the face-centered positions of the unit cell, while the element present in lower concentration (in this case, Al) occupies the corner (vertex) sites.

Elements that commonly occupy the corner positions in γ′ unit cells include Al, Fe, Nb, Ti, and Co, whereas elements that typically occupy the face-centered positions include Ni, Cr, Fe, and Co. Titanium and cobalt may occupy both types of crystallographic sites, depending on composition and processing conditions [60,51].

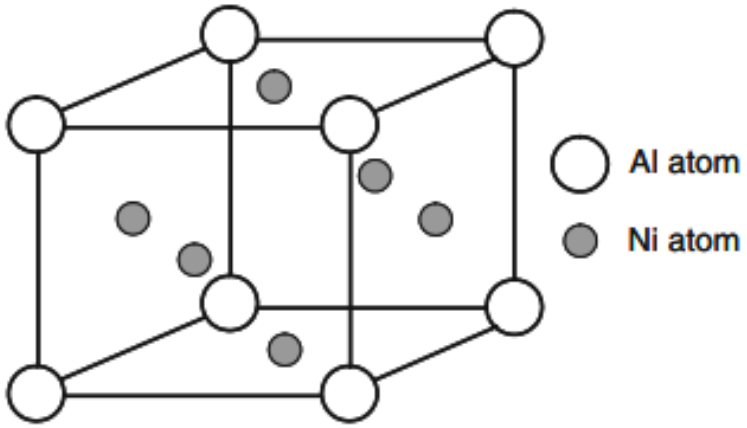

Figure 3.6: $L1_2$-type crystal structure representing the γ´-phase precipitates. The example shown here considers Ni and Al, but other elements can occupy the positions corresponding to the atoms mentioned [59].

The morphology of precipitates can vary depending on the thermal history as well as its composition. For instance, Figures 3.7 and 3.8 below show the morphology of the $L1_2$ precipitates in two different Ni-superalloys, demonstrating that the shape and size distributions of these particles can vary greatly.

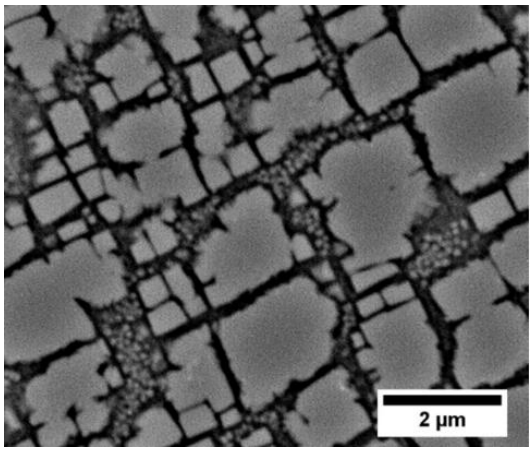

Figure 3.7: Scanning electron microscopy (SEM) image showing the precipitates of a Ni-superalloy with a composition of $Cr_{11.36}$ $Co_{8.8}$ $W_{8.19}$ $Al_{6.36}$ $Ta_{3.55}$ $Hf_{1.5}$ $Ti_{0.75}$ $Mo_{0.45}$ $C_{0.07}$ $B_{0.015}$ $Zr_{0.0125}$ $Ni_{58.9425}$ [65].

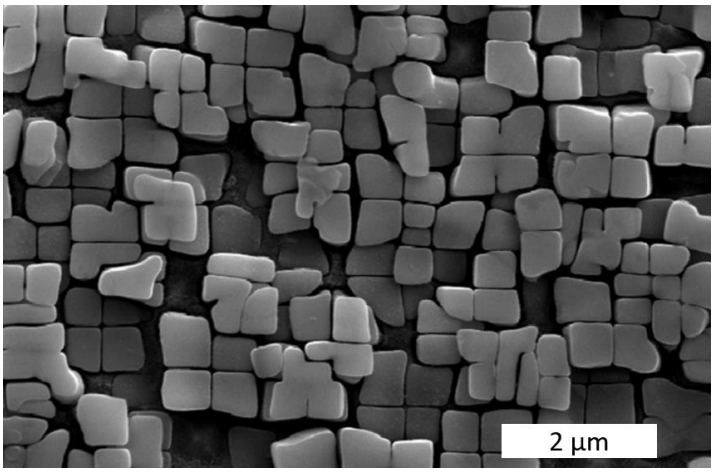

Figure 3.8: Scanning electron microscopy (SEM) image. An example of cuboidal γ´ precipitates in a Ni-superalloy. Adapted from [68].

The γ″ (gamma double prime) phase is another common type of precipitate found in Ni-based superalloys. Similar to the γ′ phase discussed previously; it exhibits a Ni_3X stoichiometry. The fundamental distinction between the γ′ and γ″ phases lie in their crystal structures. While γ′ adopts the $L1_2$ structure, γ″ crystallizes in the $D0_{22}$ structure, which corresponds to a body-centered tetragonal arrangement. This structure can be described as an ordered stacking of two FCC unit cells, in which nickel atoms occupy the face-centered positions as well as the midpoints of the unit cell edges, whereas the vertex positions and the central site of the unit cell are occupied by the X element. A representative example of this type of precipitate in Ni-based superalloys is the Ni–Nb γ″ phase.

The γ″ phase is typically present in significant volume fractions and contributes substantially to the mechanical properties of Fe-rich superalloys containing elements such as Nb. A well-known example of a superalloy whose properties are strongly associated with γ″ precipitation is INCONEL 718 [69].

Topologically close-packed (TCP) phases [70] represent another class of precipitates that may form in excessively aged alloys and are characterized by particularly complex crystal structures. Common examples of TCP phases include the σ (sigma), Laves, and η phases. These phases are generally detrimental to superalloy performance, as they tend to be brittle and sequester alloying elements that would otherwise enhance mechanical properties if retained in the matrix or in strengthening precipitates.

Carbides and borides are also important microconstituents in superalloys, primarily due to their role in enhancing creep resistance [64]. They act as effective pinning sites for grain boundaries and can additionally hinder cross-slip processes when activated at elevated temperatures.

The σ phase, a representative example of a topologically close-packed phase, exhibits a complex Frank–Kasper-type crystal structure [70]. It crystallizes in the $P4_2/mnm$ space group and has a body-centered tetragonal unit cell. Although this phase is characterized by high hardness, it is also inherently brittle, which often leads to a degradation of the mechanical properties of alloys in which it forms.

The strengthening and thermal stability mechanisms operating in high-entropy superalloys are largely analogous to those observed in conventional superalloys. For instance, increasing the nickel content above approximately 35 at.% in these alloys, as in traditional superalloys, promotes a higher γ′ precipitate fraction and enhances thermal stability. Moreover, both material classes exhibit similar optimal γ′ volume fractions, typically on the order of 70%, highlighting the close metallurgical relationship between high-entropy and conventional superalloys.

3.2.5 PRECIPITATION KINETICS

The models commonly used to describe precipitation phenomena in Ni-based superalloys are rooted in the Ostwald ripening concept, which predicts that precipitate growth proceeds in a manner that minimizes the overall interfacial energy of the system. As precipitates grow, the relative contribution of surface

area decreases compared to the increase in volume, thereby reducing the energetic penalty associated with interfaces.

More advanced mathematical descriptions of precipitation kinetics in Ni-based superalloys are provided by theories such as the Lifshitz–Slyozov–Wagner (LSW) theory [71,72]. This framework relates precipitate size to a growth rate that depends on several parameters, most notably the interfacial energy between the coexisting phases. Subsequent modifications to the original LSW formulation, such as those proposed by Ardell [73], further refine the model by explicitly relating particle size to time and by providing expressions for the precipitate growth rate, as described by the following equation:

$$r^3 - r_0^3 = Kt \qquad \text{Equation 1}$$

In this equation, r is the average particle radius at time t, and r_0 is the average particle radius at time t=0. The term k, corresponding to the particle growth rate, is given by the following expression with corrections already made to the LSW model:

$$K(f_v) = \frac{6\gamma DCeVm^2\rho m^3}{vRT} \qquad \text{Equation 2}$$

In this expression, γ represents the interfacial energy between the matrix and the precipitates, f_v is the precipitate volume fraction, D denotes the diffusivity, C_e is the equilibrium solute concentration, V_m is the molar volume of the precipitates, R is the universal gas constant, and T is the absolute temperature. The remaining terms in the equation, expressed as $F(f_v)$, correspond to mathematical functions involving the precipitate volume fraction. As indicated by this relationship, the interfacial energy is a key parameter governing precipitate growth kinetics and, consequently, their final size.

The morphology of precipitates is also strongly influenced by the interfacial energy between the precipitates and the matrix. The interplay between interfacial energy and lattice misfit energy leads to variations in precipitate shape. In

particular, when misfit energy increases significantly during precipitate growth, it may drive precipitate splitting into smaller particles [74].

Several approaches have been proposed to estimate interfacial energies in binary and multicomponent alloys containing coherent precipitates. For instance, Cahn and Hilliard et al. [47] developed a method to estimate the interfacial energy between a matrix and coherent precipitates based on concentration gradients across the interface and the associated free-energy gradient. Alternative methods have also been proposed, such as that developed by Kaptay et al. [67], which enables interfacial energy estimation without requiring concentration or energy gradients at the interface, nor parameters such as interface thickness. In addition to interfacial energy, time is a critical parameter in precipitate evolution, as precipitate size may follow different kinetic laws depending on heat-treatment conditions, often scaling with the cube of the aging time [94].

This sensitivity is clearly demonstrated in computational precipitation simulations performed using the PanEvolution module of the Pandat® software [46]. For example, simulations carried out for a multicomponent alloy with the composition $Cr_{29.7}Co_{29.7}Ni_{35.4}Al_{4.0}Ti_{1.2}$, consisting of an FCC matrix and $L1_2$ precipitates, revealed that variations in interfacial energy have a pronounced effect on precipitation behavior. Specifically, changing the interfacial energy from 15 to 48 $mJ \cdot m^{-2}$ resulted in substantial differences in particle size distribution.

The strong dependence of precipitate characteristics—such as average radius and size distribution—on interfacial energy underscores the importance of accurately determining interfacial energy values for the microconstituents of metallic systems of interest. However, this task is far from trivial, as direct experimental determination of interfacial energies is highly challenging. Experimental techniques such as atom probe tomography [77] are therefore often employed in combination with complementary computational approaches. This further emphasizes the need for reliable computational methods capable of providing interfacial energy values.

One such computational approach is the generalized broken-bond model [78], which estimates interfacial energy based on the number of broken nearest-

neighbor bonds at the interface. This model is implemented in an embedded form within CALPHAD-based software packages, such as Pandat®, for estimating interfacial energies. However, it relies on parameters derived from prior calculations, which may vary depending on the specific material system under investigation. An alternative and more general approach for calculating interfacial energies in metallic systems is the use of first-principles (ab initio) methods, particularly Density Functional Theory (DFT). In these methods, minimal prior information about the system is required, and the range of possible calculations is broad and versatile.

The present study is further motivated by the relevance of ab initio approaches in the context of high-entropy superalloys (HESAs). As highlighted by Varvenne et al. [102], the identification of promising HESA compositions relies heavily on high-throughput computational screening, which in turn requires key thermodynamic and interfacial parameters obtained from first-principles calculations. This clearly demonstrates the critical role of DFT as a foundational tool for subsequent superalloy modeling and simulation efforts.

3.2.6 DENSITY FUNCTIONAL THEORY

Computational simulation tools play a central role in the design and development of engineering materials, including metallic alloys. Methods such as CALPHAD, molecular dynamics, and the finite element method [67,80] enable the prediction of material behavior through the simulation of thermodynamic, structural, and mechanical properties. The application of computational approaches in materials science expanded significantly during the 1980s and 1990s with the emergence of software packages such as CHARMMS [68,81] and VASP [69,82], which facilitated studies on biomaterials [70,83] and the electronic properties of solids [71,84]. These advances highlighted the importance of atomistic-scale simulations for determining fundamental quantities such as lattice parameters, total energies, and electronic structures.

Density Functional Theory (DFT), hereafter referred to simply as DFT, provides a quantum-mechanical framework for predicting material properties based on the electronic density functional. Originating from theoretical

developments in the 1950s and 1960s, DFT has become a widely used simulation technique for investigating magnetic behavior, interface engineering [84,85], corrosion processes, and optical and thermodynamic properties [76,82]. Moreover, DFT is frequently coupled with complementary approaches such as machine learning [75,96] and molecular dynamics to extend its predictive capabilities.

In the context of metallic alloys, DFT is commonly employed to evaluate elastic constants, mechanical behavior [72,86], as well as electronic [71,84], thermal [73,87], and optical properties [79,95], thereby providing valuable insights for alloy design and optimization. Since these properties are governed by fundamental atomic arrangements, ab initio approaches such as DFT are particularly advantageous due to their minimal dependence on empirical parameters. Representative examples include the work of Ouadah et al. [79,95], who investigated the elastic properties of Al–Ti alloys with transition-metal additions using DFT-calculated lattice parameters and density-of-states (DOS) analyses to assess electronic contributions to electrical conductivity.

Another important application of DFT is the calculation of interfacial energies, including free surface energies and phase-boundary energies. In Ni-based superalloys, for example, DFT has been successfully employed to compute antiphase boundary (APB) energies. Dodaran et al. [52,61] demonstrated this capability by examining the influence of alloying elements on APB energies in precipitates relevant to Ni-based superalloys.

3.2.6.1 DFT FUNDAMENTALS

A classical particle system can be fully described by Newton’s laws of motion, in which the positions, velocities, and accelerations of particles are determined explicitly from the interactions among the objects in the system. In contrast, these classical principles are inadequate for describing behavior at the subatomic scale. For systems involving electrons and nuclei, the appropriate theoretical framework is provided by the Schrödinger equation (Eq. 3), which plays a role analogous to that of Newton’s equations in classical mechanics. In

principle, an exact solution of the Schrödinger equation would yield a complete description of the quantum system. In Schrödinger equation, H is the hamiltonian operator, Ψ is the wave function describing the system and E the energy associated with the system.

$$H\Psi = E\,\Psi \qquad \text{Equation 3}$$

In practice, solving the Schrödinger equation for realistic many-body systems is computationally intractable due to the complexity of the Hamiltonian, which includes contributions from electron kinetic energy, nuclear kinetic energy, electron–nucleus interactions, nucleus–nucleus interactions, and electron–electron interactions (Eq. 4). In Eq.4, $\widehat{\mathrm{H}}$ is the Hamiltonian, N and M are integers, r, R and Z represent, respectively, specific electrons positions, nuclei positions and electric charges of nuclei. ∇ represents the Laplacian operator for kinetic energy. This intrinsic complexity has motivated the development of alternative theoretical and computational approaches for the determination of material properties.

$$\widehat{\mathrm{H}} = -\frac{1}{2}\sum_{i=1}^{N}\nabla_i^2 \; -\frac{1}{2}\sum_{j=1}^{M}\frac{1}{M_j}\nabla_j^2 \; -\sum_{i=1}^{N}\sum_{j=1}^{M}\frac{Z_j}{|r_i - R_j|} + \sum_{j=1}^{M}\sum_{k>j}^{M}\frac{Z_j Z_k}{|R_j - R_k|} + \sum_{i=1}^{N}\sum_{j>i}^{N}\frac{1}{|r_i - r_j|}$$

Equation 4

A major conceptual breakthrough was provided by the two Hohenberg–Kohn theorems. The first theorem (1964) [74,88] establishes that the ground-state electronic density uniquely determines all properties of a many-electron system, introducing fundamental concepts such as the exchange–correlation energy. The second theorem (1965) [75] formulates a variational principle stating that the ground-state energy is minimized with respect to the electronic density, thereby enabling practical numerical minimization procedures. Together, these theorems form the foundation of Density Functional Theory (DFT), whose central premise is that all ground-state quantum-mechanical properties can be expressed as functionals of the electronic density.

Nevertheless, the Hohenberg–Kohn theorems alone do not eliminate the computational challenges associated with solving the Schrödinger equation. As a result, additional approximations are required, giving rise to practical frameworks such as the Hartree–Fock method and modern implementations of DFT. Another key simplification is the Born–Oppenheimer approximation, in which the nuclei are treated as classical particles. This approximation reduces the complexity of the Hamiltonian by neglecting nuclear kinetic energy terms and simplifying electron–nucleus interactions (Eq. 5).

$$\widehat{H}_e = -\frac{1}{2}\sum_{i=1}^{N}\nabla_i^2 - \sum_{i=1}^{N}\sum_{j=1}^{M}\frac{Z_j}{|r_i - R_j|} + \sum_{i=1}^{N}\sum_{j>i}^{N}\frac{1}{|r_i - r_j|}$$

Equation 5

With this reformulation, the problem shifts from determining the many body wavefunction to finding the electronic density, thereby enabling tractable approximate solutions for material properties. In Eq.5, $\widehat{\mathrm{He}}$ is the approximated Hamiltonian, N and M are integers, r, R and Z represent, respectively, specific electrons positions, nuclei positions and electric charges of nuclei and ∇ represents the Laplacian operator for kinetic energy.

The Kohn–Sham method represents a major conceptual advance in the treatment of the many-body Schrödinger equation. In the 1960s, Kohn and Sham proposed replacing the real interacting many-electron system with an equivalent fictitious system of non-interacting particles that reproduces the same ground-state electronic density as the original system. As a result, instead of solving the full many-body problem, one solves a set of single-particle equations whose solutions are combined self-consistently to recover the total electronic density.

The self-consistent procedure begins with an initial guess for the electronic density. From this density, an effective potential is constructed and used to solve the Kohn–Sham equations for each particle, yielding an updated electronic density. This cycle is repeated iteratively until convergence is achieved. Once self-consistency is reached, relevant system properties, such as total energy and atomic forces, can be evaluated.

This reformulation renders the problem computationally feasible; however, it introduces an inherent limitation. The fictitious non-interacting particles experience an effective potential that differs from that of the real interacting system. The missing many-body effects are accounted for through the exchange–correlation energy, which is described by an exchange–correlation functional. Since the exact functional is unknown, practical implementations rely on approximate forms. The most commonly used approximations include:

Local Density Approximation (LDA): Assumes that the electronic density at each point behaves locally as a uniform electron gas. This approximation is most accurate for systems with slowly varying electronic densities.

Generalized Gradient Approximation (GGA): Incorporates gradients of the electronic density, improving accuracy for systems with significant spatial variations. Widely used functionals, such as PBE, belong to this class.

Meta-GGA (MGGA): Extends GGA by including higher-order terms, such as the Laplacian of the density or kinetic energy density, offering improved accuracy at the expense of increased computational cost.

Adiabatic Connection Method (ACM): Hybrid approaches that combine exact exchange from Hartree–Fock theory with DFT correlation, potentially enhancing accuracy across a broad range of systems, although their implementation is less common in some DFT codes.

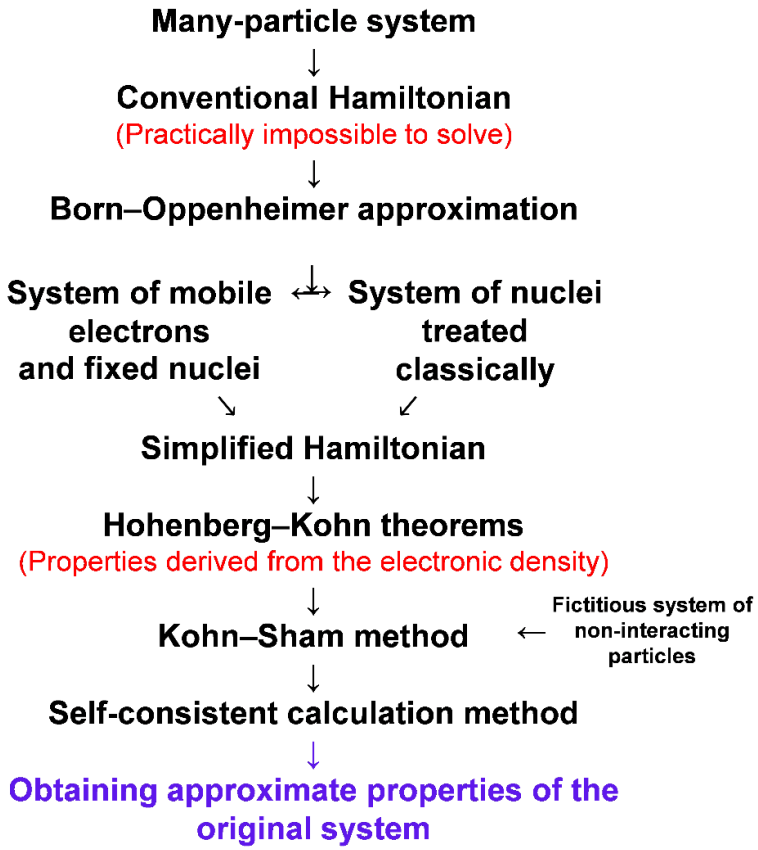

Figure 3.9: Scheme showing the sequence of steps involved in DFT calculations.

Together, the Hohenberg–Kohn theorems and the Kohn–Sham framework enable practical computation of electronic densities through a self-consistent algorithm. Once converged, the method yields key material properties such as total energy, forces, and other observables relevant to quantum-mechanical materials modeling.

3.2.6.2 IMPORTANT PARAMETERS IN DFT CALCULATIONS

Smearing Functions: Smearing is a numerical technique employed in DFT calculations to smooth abrupt changes in the electronic occupation of states in solids. The differences among smearing schemes arise from the specific mathematical form used to broaden the electronic transitions. The application of smearing functions enhances numerical stability, particularly for systems with

electronic states near the Fermi level. Commonly used smearing schemes include:

→Fermi–Dirac (FD)

→Gaussian (Gauss)

→Methfessel–Paxton (MP)

→Marzari–Vanderbilt (MV)

Reciprocal-Space Grid (k-point Mesh): DFT calculations performed on unit cells or supercells require sampling of reciprocal space, which represents the periodicity of the crystal through the reciprocal lattice. Within this framework, concepts such as the Brillouin zone—corresponding to the unit cell in reciprocal space—are defined. The k-point mesh specifies the number and distribution of points used to sample the reciprocal-space unit cell. Increasing the number of k-points generally improves accuracy, albeit at the expense of higher computational cost. For cubic or orthorhombic cells, the reciprocal lattice vectors scale inversely with the real-space lattice parameters. Consequently, if a real-space lattice has a = b and c = 3a, the reciprocal lattice vector along the c direction is one-third the magnitude of the others, and the number of k-points sampled along this direction should follow the same proportionality.

Cut-off energy: it defines the maximum kinetic energy of plane waves included in the basis set used to represent electronic wavefunctions. Higher cutoff energies generally lead to more accurate results but significantly increase computational cost. In practice, two cutoff values are commonly employed: a lower cutoff for the wavefunctions and a higher cutoff for the charge density, the latter typically set to approximately four times the former.

Pseudopotentials: Are fictional potentials that approximate the interaction between valence electrons and ionic cores, enabling the exclusion of core electrons from the calculation and thereby reducing computational cost. Various types of pseudopotentials are available to represent different electronic configurations and levels of accuracy [77,78,89,90].

Convergence tests: Convergence testing is a fundamental step in DFT simulations to ensure both numerical reliability and computational efficiency. During these tests, key input parameters—such as cutoff energies, pseudopotentials, k-point meshes, and smearing schemes—are varied systematically while monitoring the total energy. Convergence is achieved when further changes in these parameters no longer produce significant variations in the total energy. This procedure is essential because initial parameter choices may lead to unstable or erratic total-energy behavior. Establishing convergence ensures numerical stability while identifying the minimum parameter values required to obtain accurate and reliable results at an optimized computational cost.

3.2.6.3 DFT IN CALCULATIONS OF INTERFACIAL ENERGIES

Density Functional Theory (DFT) enables the calculation of interfacial energies between distinct phases in metallic systems. An example of a supercell containing both the matrix and precipitate phases is shown in Figure 3, in which nickel atoms are represented in blue and aluminum atoms in pink. In this configuration, a vacuum layer is introduced to separate periodic images of the interface, preventing spurious interactions between them [83,90].

Using this approach, the authors employed DFT to investigate the segregation behavior of Cr, Co, Re, Nb, Zr, Hf, Ta, Ru, Y, Ti, Mo, and W at Ni–Ni_3Al interfaces, allowing these elements to occupy atomic sites within both the matrix and the interfacial region. The results revealed clear correlations between elemental segregation tendencies and mechanical properties, particularly fracture toughness.

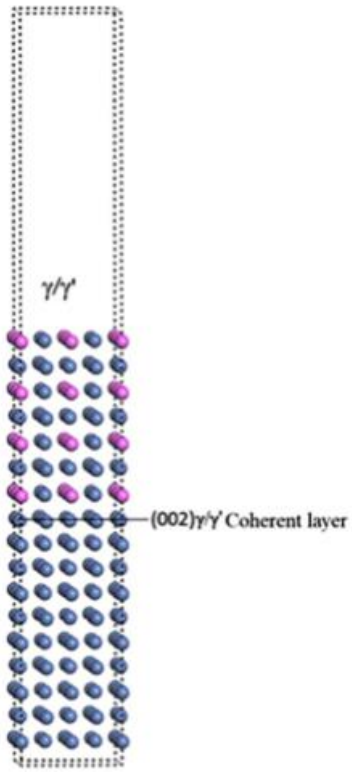

Figure 3.10: Example of supercell used to perform interfacial energies calculations [83,90].

Their methodology employs supercells containing both phases and the corresponding interface, as well as separate supercells representing the individual pure phases. The interfacial supercell is constructed by extending the unit cells along the a and b directions and stacking at least three-unit cells of each phase along the c direction. The lattice parameter is typically taken as the arithmetic mean of the lattice parameters of the matrix and the precipitate. To avoid spurious interactions between periodic images, a vacuum layer is introduced, with its thickness selected based on convergence tests or values reported in the literature.

Other studies, including those by Wang et al. [84,85], adopt similar strategies but place vacuum layers on both sides of the slab. In addition, formulations for systems composed of phases A and B have been proposed [84, 85,91,92]. In these approaches, the interfacial energy is calculated from the difference between the total energy of the combined-phase supercell ($E_{A/B}$) and

the energies of the isolated matrix and precipitate supercells (E′$_A$ and E′$_B$>, respectively), normalized by the interfacial area.

This approach rises as the main path to calculate interfacial energies trough density functional theory, using three supercells for each energy calculation. One problem that may arise from this formulation, as it will be seen is that it is possible that the size of the system introduces errs in the calculations due to a multi-slab effect.

$$\gamma = \frac{E_{A/B} - \frac{E'A + E'B}{2}}{A}$$

Equation 6

Chandran et al. [75,96] proposed a regression-based machine-learning approach combined with Density Functional Theory (DFT) to compute γ′/matrix interfacial energies in Ni-617 superalloys. In contrast to most previous studies, which commonly approximate the matrix as pure FCC Ni, their work treats the matrix as a true multicomponent solid solution, thereby providing a more realistic representation of industrial alloy systems. Different methods and input parameters for DFT calculations can greatly change results. For reference, interfacial energies DFT calculations of Ni–Ni_3Nb interfaces employing different input parameters and software lead to results ranging from 1mJ/m^2 to hundreds of J/m^2 [96].

Extending interfacial energy calculations to such realistic compositions necessitates the construction of compositionally accurate supercells. This requirement can be fulfilled by coupling DFT calculations with structure-generation techniques, such as Monte Carlo molecular dynamics (MCMD), enabling the generation of statistically representative atomic configurations for multicomponent alloys.

3.3 MATERIALS AND METHODS

3.3.1 CHOICE OF COMPOSITIONS

To select the alloy composition investigated in this work, high-throughput thermodynamic calculations were performed using the Pandat® software. This approach enables the exploration of extensive compositional spaces in order to identify specific compositions that exhibit targeted characteristics. In the present study, the primary features of interest are the presence of $L1_2$-ordered precipitates within a disordered FCC matrix.

More specifically, the compositional selection was based on the following criteria:

I – Only compositions that maintained single-phase FCC stability at elevated temperatures (1100 °C) were considered for further evaluation.

II – The phase diagrams of the selected compositions must exhibit at least one temperature range in which FCC coexists with $L1_2$ and/or $D0_{22}$ phases, within a temperature window between 650 °C and 800 °C.

III – The combined volume fraction of the $L1_2$ and $D0_{22}$ phases must be equal to or less than 0.5, while satisfying criterion II.

In addition, the compositional ranges adopted for each alloying element constitute an additional selection criterion. These ranges are summarized in Table 3.1. The quantities of each element shown come from previous works of our team and are based on the typical ranges of elements present in superalloys.

Table 3.1: Compositional space of Ni based superalloys that was used in this work.

Element	%at min	%at max	△%
Cr	10.0	25.0	2.5
Co	0.0	20.0	5.0
Al	0.0	10.0	2.5
Ti	0.0	5.0	2.5
Nb	2.5	7.5	2.5
Fe	0.0	40.0	20
Ni	30.0	70.0	-----

Considering all those criteria reported above, High throughput calculations performed led to 76 possible candidates. The selected compositions were then ranked based on a combination of predicted properties, including mechanical strength, toughness, and corrosion resistance. In addition, other relevant factors, such as the cost and availability of the constituent elements, were considered in the selection of the alloy investigated in this work. Based on these factors, as well as on the previously stated selection criteria, the composition ultimately chosen over the others was: $Cr_{12.5}Al_{2.5}Ti_{5.0}Nb_{2.5}Fe_{20.0}Ni_{57.5}$.

The solidification simulation for this composition, obtained by Thermo-Calc® is shown below, illustrating the equilibrium phase evolution. Although phases other than FCC and $L1_2$ are predicted by the simulation, under experimental conditions— as discussed later—only these two phases are observed to form in the alloy.

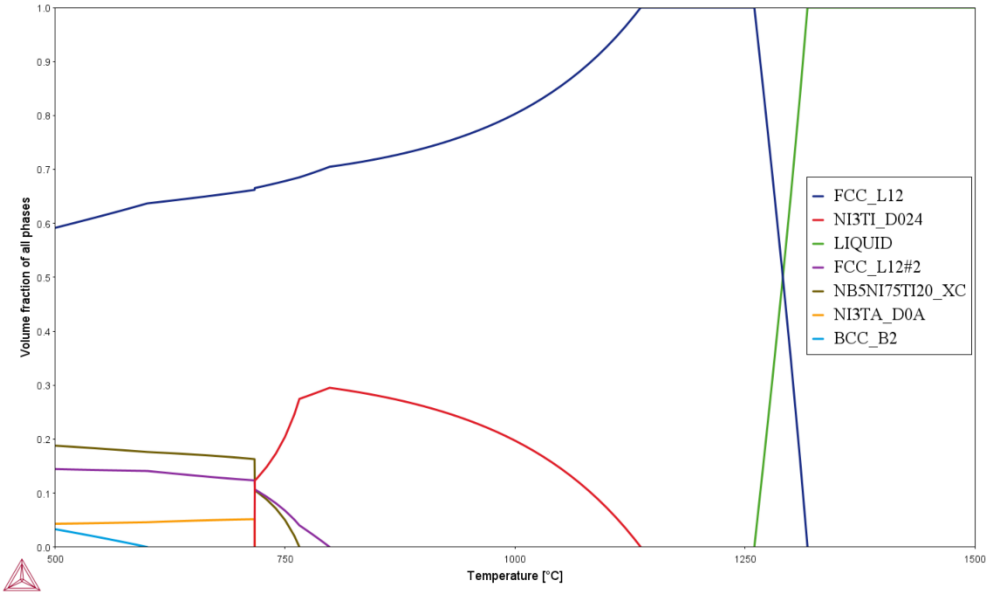

Figure 3.11: Solidification simulation for the chosen alloy showing the presence of FCC, $L1_2$ and other phases (those do not form in experimental conditions due to kinetics) obtained using TCHEA5 database in Thermo-Calc®.

3.3.2 MATERIAL PRODUCTION

The selected composition (Section 3.4.1) was produced using a **Vacuum Induction Melting (VIM)** furnace (model GCA, Vacuum Industries) under an argon atmosphere. Two ingots were produced for this composition, and each ingot was remelted at least five times to ensure chemical and microstructural homogeneity.

3.3.3 PRECIPITATION TREATMENT

The as-cast alloy was subsequently remelted using an arc-melting process. The material then underwent a homogenization treatment at 1200 °C for 8 hours, followed by cold rolling to a thickness reduction of 70%. Subsequently, the alloy was annealed at 1150 °C for 1 hour to promote recrystallization and ensure the dissolution of secondary phases within the matrix. The final heat-treatment step consisted of aging at 750 °C for 1 hour, followed by water quenching.

3.3.4 X-RAY AND SYNCHROTRON DIFFRACTION

To investigate the phases, present in the alloy, X-ray diffraction (XRD) analyses were performed using a Bruker D8 Advance ECO diffractometer. The instrument operates with a characteristic Cu–Kα_1 radiation (λ = 1.54 Å, 8.047 keV) and a 2θ scanning range from 5° to 120°. In addition, synchrotron X-ray diffraction (S-XRD) experiments were carried out at the Deutsches Elektronen-Synchrotron (DESY), located in Bahrenfeld, Hamburg, Germany, using the PETRA III P07 beamline. These measurements were conducted at a fixed photon energy of 102.85 keV, corresponding to an X-ray wavelength of 0.12055 Å.

The diffraction patterns obtained from the synchrotron experiments were processed using Python-based routines to determine the volume fractions of the phases present. The analysis procedure is described as follows. First, the two-dimensional Debye–Scherrer rings were converted into conventional one-dimensional intensity versus 2θ diffraction patterns by azimuthal integration over the full angular range (φ = 0–360°), using a combination of Python-based tools [103]. Individual diffraction peaks were then fitted using a pseudo-Voigt function to extract key parameters, including peak position, intensity, full width at half maximum (FWHM), and integrated peak area.

The volume fraction of the $L1_2$ phase was calculated based on the integrated area of the $L1_2$ (100) reflection, which is the only diffraction peak exclusive to the $L1_2$ phase in the diffractogram. This area was normalized by the area of the most intense peak in the pattern, corresponding to the superposition of the FCC (311) and $L1_2$ (311) reflections. Theoretical relative intensities were employed to deconvolute the respective contributions of the FCC and $L1_2$ phases within this composite (311) peak.

3.3.5 CALCULATION OF INTERFACIAL ENERGIES TROUGH DFT

To perform such interfacial energy calculations, the system containing matrix, precipitate and the interface is described using supercells. A general model for one of those is shown in figure 3.12. The supercells used corresponds to a cell with a and b lattice parameter maintained and the c lattice parameter increased.

To calculate the interfacial energies, two main strategies were employed. The first strategy, based on Density Functional Theory (DFT), consists of an ab initio approach to compute the energies of alloy systems with and without interfaces representative of those formed between FCC and $L1_2$ phases. This approach is entirely computational and was carried out using the Quantum ESPRESSO and VASP software packages.

The procedure involved systematic convergence tests to determine appropriate simulation parameters. In general, convergence testing consists of varying a single parameter while keeping all others fixed, and identifying the minimum value of the varying parameter that leads to stable total-energy values for the system. Convergence tests were first performed to select suitable pseudopotentials for all alloying elements. Subsequently, additional convergence tests were conducted to determine optimal values for parameters relevant to interfacial energy calculations, such as k-point meshes, plane-wave cutoff energies, and other key DFT settings.

Another critical parameter in DFT-based interfacial energy calculations is the size of the supercell used to model the interface between the matrix and the $L1_2$ phase. This constituted the final convergence test, in which the interfacial energy was evaluated as a function of the number of atoms included in the supercell. The results of this analysis allowed the identification of the converged interfacial energy value of interest.

To perform these interfacial energy calculations, systems containing the matrix, the precipitate, and the interface were described using supercells. A representative model of such a supercell is shown in Figure 3.12. The supercells employed maintain the lattice parameters a and b fixed, while the lattice parameter c is increased to accommodate the interfacial region.

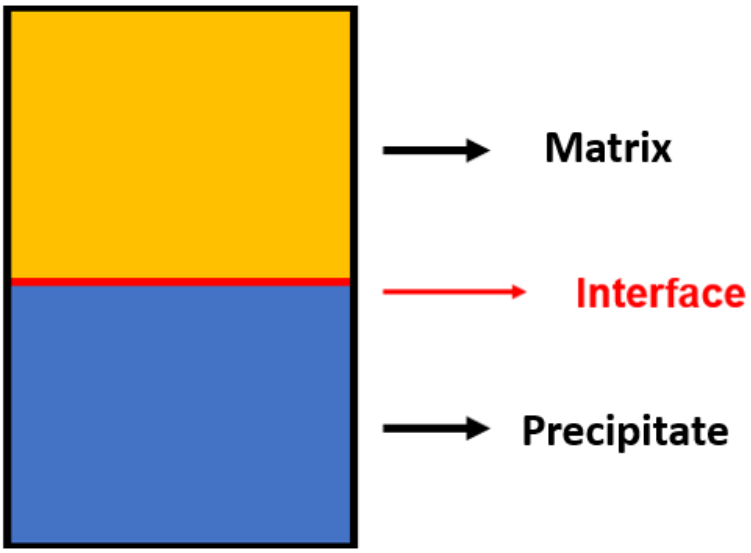

Figure 3.12: Prototype of supercell to be used to perform DFT calculations of interfacial energy for Ni-Ni3al. This supercell contains both phases. Two additional supercells, one containing only Ni3Al and on only containing Ni were also built.

As it is shown, the supercell consists of two regions of equal sizes: one of them represents a pure Ni matrix and the other, Ni_3X precipitate, being X Al or Ti for example. It was chosen to perform the calculations without vacuum to facilitate the calculations and constructions of supercells and because it seemed to insert a free surface in the system. To investigate the interfacial energy between the matrix and precipitates in a multicomponent alloy, different supercells were constructed to represent the various possible combinations of elements in the matrix and in the precipitate. This approach enables the extrapolation of the calculated interfacial energy values to arbitrary compositions involving the selected elements. In addition to the interfacial supercells, two additional types of supercells were generated for each interfacial energy calculation: one containing only the matrix phase and another containing only the $L1_2$ phase.

3.3.6 ALTERNATIVE APPROACH FOR ESTIMATING INTERFACIAL ENERGIES.

An alternative approach for calculating interfacial energies involves a semi-empirical procedure that combines Rietveld refinement, in situ dilatometry, and synchrotron diffraction analyses. In this method, thousands of diffraction patterns obtained under different time and temperature conditions during a precipitation cycle are analyzed to generate data describing the evolution of the $L1_2$ phase fraction throughout the heat treatment. Complementary information can be obtained from measurements of sample dilation during the same precipitation cycle. Together, these datasets enable the construction of continuous cooling transformation (CCT) diagrams for the alloys of interest.

Once generated, these CCT diagrams can be compared with CALPHAD-based precipitation simulations to estimate interfacial energies, which serve as key input parameters in such simulations. This procedure represents a “reverse” modeling strategy, in which experimental observations are used to calibrate and refine thermodynamic and kinetic simulation parameters, thereby integrating experimental data with computational modeling.

Precipitation simulations were performed using the PanEvolution module of the Pandat® software. This software consists in an add-on that allows Pandat® do perform kinetic-like simulations such as precipitation simulations. This process works by inputting parameters such as the heat-treatment information of a determined process of interest. For example: in the present case, the in-situ dilatometry conditions of time and temperatures were put as input parameters for the precipitation simulations. The software allows to estimate information like volumetric fractions and chemical compositions of a determined precipitate at any step of the thermal treatments. Figure 3.19 thermal treatment was simulated and information of the characteristics of the precipitates were obtained ad the end of the cooling “C1” shown in the figure 3.19.

To perform such calculations, there is the necessity of using a combined set of kinetic and thermodynamic databases. The simulations employed the “Thermodynamics + Mobility’s Nickel” database provided by Pandat®, which provides thermodynamic and kinetic data representative of Ni-based superalloys.

In these calculations, various parameters have default values but are adjustable. Pre-set definitions used for traditional Ni-based superalloys were used. The only parameter not taken as its default value as the interfacial energy (the Default value is 35 mJ/m2). To analyze the interfacial energy influence on the precipitates´ characteristics, this parameter was treated as the sole adjustable input parameter and was varied over a range from 5 to 95 $mJ \cdot m^{-2}$. As mentioned, the experimentally applied thermal treatments were used to define the corresponding time–temperature profiles in the simulations. The simulation outputs consisted of the predicted $L1_2$ volume fraction as a function of time, temperature, and interfacial energy. As mentioned, the end of C1 cooling was the region chosen to make the simulations. Summarizing: The experimental conditions shown in figure 3.19 up to the end of C1 cooling were replicated in kinetic simulations using Pan-precipitation software using databases suitable for Ni-based superalloys. The interfacial energy between FCC matrix and L12 matrix were varied from 5-95 mJ/m2 and the main output was the volumetric fractions of L12 precipitates after C1 cooling. Those values of volumetric fraction were compared to correspondent volumetric fractions obtained experimentally to estimate which interfacial energy leads to most accurate simulations.

The dependence of the volumetric fraction of L12 obtained via simulation and the interfacial energy is presented in Figure 3.20 and was subsequently compared with the phase-fraction values determined experimentally from diffraction peak integration.

3.4 RESULTS AND DISCUSSION

3.4.1 DFT SIMULATIONS: RESULTS OF CONVERGENCE TESTING

After performing convergence tests for the input parameters, the optimal values for the k-point mesh, plane-wave cutoff energy, pseudopotentials, and smearing function were determined. As previously mentioned, the convergence-testing procedure consists of varying a single parameter while keeping all others fixed and monitoring the corresponding changes in the total energy of the system.

The first set of calculations focused on identifying the most suitable pseudopotential for each alloying element. The selection of pseudopotentials is

a critical initial step, as it would be inconsistent to optimize other input parameters for one pseudopotential and subsequently verify their suitability for a different one.

For the convergence tests involving different pseudopotentials, the adopted strategy was to evaluate their ability to reproduce the lattice parameter of a simple unit cell for each pure element considered in this study. To this end, an initial lattice parameter different from the experimental value was assigned to each elemental unit cell. Subsequently, a series of structural relaxation calculations were performed, each employing a different pseudopotential, to determine the equilibrium lattice parameter. The pseudopotential that yielded a lattice parameter closest to the experimentally reported value for each element was selected. The results obtained from these simulations are summarized in Table 3.2 for all elements investigated in this work.

Table 3.2: converged pseudopotentials for each element of this study.

Chemical Element	Pseudopotential
Co	Co_ONCV_PBE_FR-1.0.upf
Cr	Cr_ONCV_PBE_FR-1.0.upf
Ni	Ni_ONCV_PBE_FR-1.0.upf
Al	Al.pbe-n-kjpaw_psl.1.0.0.UPF
Fe	FE_PBE_PAW.upf
Ti	TI_PBE_PAW.upf
Nb	Nb.pbe-sp-hgh.UPF.upf

Examples of convergence tests with respect to the k-point mesh are shown in Figure 3.13. Results of DFT calculations come normally in Rydeberg. Such values can be converted in Joule, as it will be shown when calculating the interfacial energies. For convergence analysis, energies can be analyzed in Rydeberg. It can be observed that the total energy of the system changes significantly as the number of sampling points in the reciprocal lattice increases from 4 to 8, after which it stabilizes at approximately −1233.150 Ry. Although the

absolute difference in total energy may initially appear small—for instance, −1233.14029882 Ry for a 4 × 4 × 4 mesh and −1233.14921927 Ry for an 8 × 8 × 8 mesh, corresponding to a difference of about 0.009 Ry—this variation becomes meaningful when analyzed in a relative context.

Specifically, when comparing this difference with that observed between an 8 × 8 × 8 and a 9 × 9 × 9 k-point mesh, it becomes evident that increasing the mesh from 4 to 8 points in each direction results in an energy change approximately 30 times larger than that associated with increasing the mesh from 8 to 9. This comparison highlights the importance of selecting a minimum k-point density that ensures the total energy remains within a well-defined and stable range. Such a choice is essential to guarantee the numerical stability and reliability of subsequent calculations with respect to the selected input parameters.

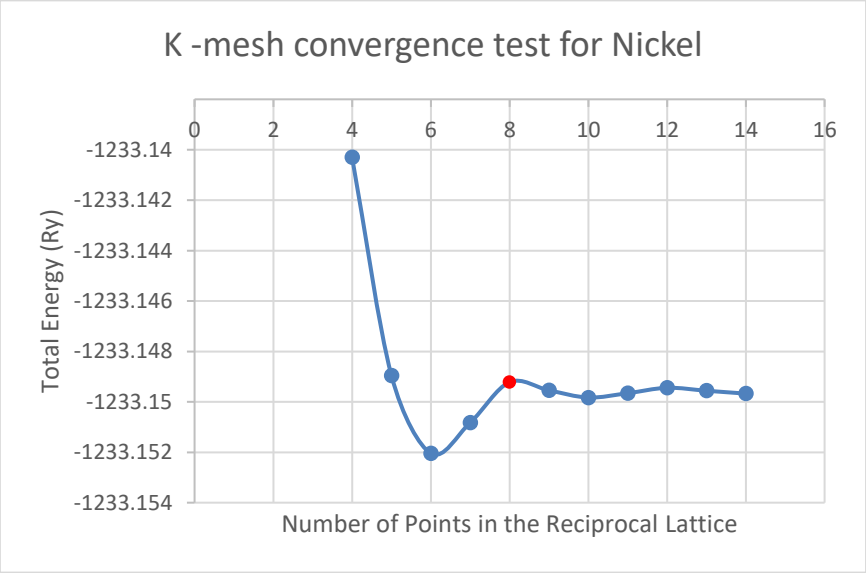

Figure 3.13: k-mesh convergence test for nickel. It is shown that energy minimally changes for values of k-mesh greater than 8.

The converged number of k-points for each element is listed in Table 3.3. It can be observed that the minimum converged values range between 7 and 11 points per reciprocal-lattice direction, yielding a weighted average of approximately 8.86 points. Based on this analysis, a k-point mesh of 10 × 10 × 10 was selected for subsequent convergence tests. This choice was motivated by the fact that a 10 × 10 × 10 mesh corresponds to a value equal to or higher

than the converged requirement for five of the seven elements considered in the simulations.

The remaining exceptions are Fe and Nb. For Fe, the converged k-point mesh was determined to be 11 × 11 × 11. However, the energy difference between a 10 × 10 × 10 and an 11 × 11 × 11 mesh is approximately 0.0004 Ry (≈ 0.005 eV), which is negligible for the purposes of the present calculations. For Nb, a 10 × 10 × 10 mesh corresponds exactly to the converged value rather than a higher one. Nevertheless, increasing the mesh from 10 × 10 × 10 to 11 × 11 × 11 results in an energy change of only about 0.0003 Ry (≈ 0.004 eV).

These results clearly indicate that a k-point mesh of 10 points in each reciprocal-lattice direction is sufficient to ensure convergence for all elements considered. Moreover, this choice can be regarded as conservative in all cases. Consequently, a 10 × 10 × 10 k-point mesh was adopted as the default input parameter for the calculations involving all seven elements.

Table 3.3: Converged number of lattice points for all the elements.

Chemical Element	Number of points in reciprocal lattice in three directions
Co	7 x 7 x 7
Cr	8 x 8 x 8
Ni	8 x 8 x 8
Al	9 x 9 x 9
Fe	11 x 11 x 11
Ti	9 x 9 x 9
Nb	10 x 10 x 10

Additional convergence tests were performed to determine appropriate values for the plane-wave cutoff energy and the smearing function. The cutoff energy was varied from 20 to 180 Ry for each element. The results indicate that energy convergence is achieved in the range of approximately 50 to 70 Ry for most elements. Nickel, for example, exhibits the energy–cutoff relationship

shown in Figure 3.14, which illustrates the stabilization of the total energy as a function of increasing cutoff energy.

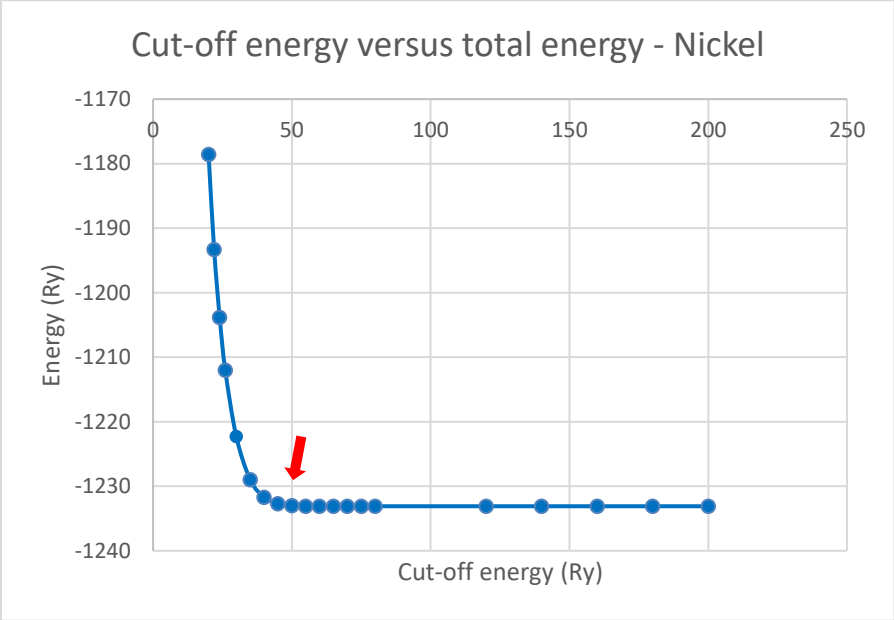

Figure 3.14: cut-off energy convergence test for Nickel

The curve indicates that the total energy of the system stabilizes at approximately 50 Ry and then remains close to −1233 Ry. This behavior was observed for all elements considered, except for Ti. For titanium, the energy–cutoff relationship exhibited a markedly different trend, as shown in Figure 3.15.

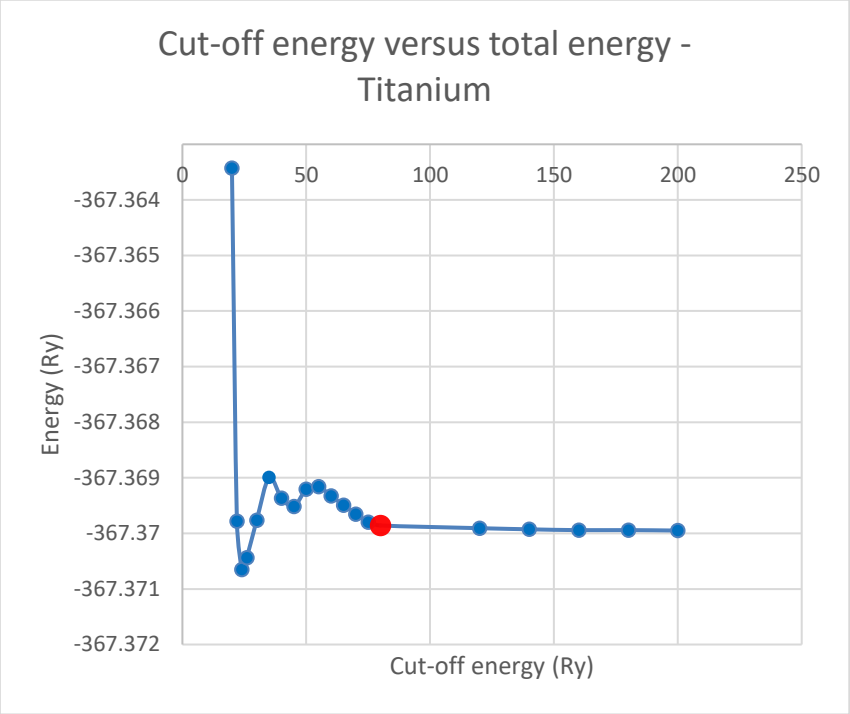

Figure 3.15: Cut-off energy convergence testing for Titanium. The value stabilizes around 80 Ry.

For titanium, the total energy of the system stabilizes only at a cutoff energy of approximately 80 Ry. Therefore, in order to adopt a conservative approach, a cutoff energy of 80 Ry was selected for calculations involving all elements.

With respect to the smearing function, the Fermi–Dirac (FD), Gaussian (Gauss), Methfessel–Paxton (MP), and Marzari–Vanderbilt (MV) schemes were tested, as shown in Figure 3.16. The results indicate that, for all elements, the MV smearing function provides the greatest energetic stability. This behavior is illustrated for chromium in the figure below, where the FD and Gaussian schemes lead to significant fluctuations in the total energy, rendering them unsuitable for the present calculations. In contrast, the MP and MV schemes yield much more stable energy values. Although the MP and MV curves appear nearly identical, a closer examination of the results revealed that the MV scheme provides slightly improved stability. Consequently, the Marzari–Vanderbilt smearing function was selected as the optimal choice for describing the smearing parameter.

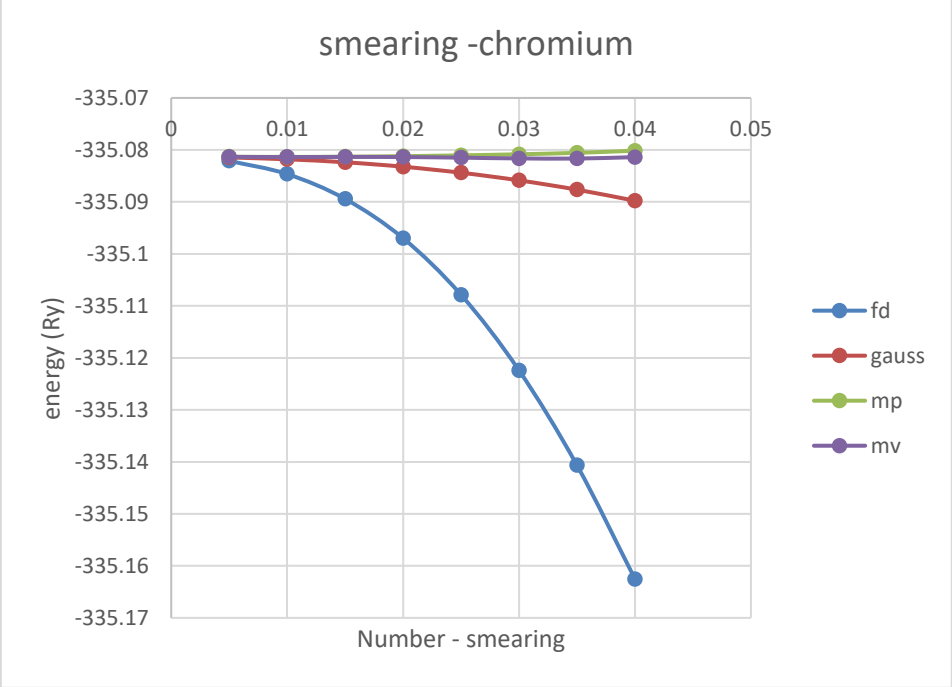

Figure 3.16: Energy changes as the number os smearing changes for each kind of smearing function: fd, gaussian, mp and mv.

After completing the convergence tests for the k-point mesh and the plane-wave cutoff energy, and to adopt a conservative approach and homogenize the input parameters across all calculations, uniform values were selected for all elements and simulations. Specifically, a 10 × 10 × 10 k-point mesh and a cutoff energy of 80 Ry were adopted.

Once the convergence tests were completed, the interfacial energy between the disordered FCC matrix and the $L1_2$ precipitate could be calculated using the converged parameters as simulation inputs. At this stage, an additional convergence test was performed to determine the appropriate supercell size. This step is critical because, as with the previously discussed convergence parameters, variations in the number of atoms in the system can significantly affect the calculated energy values. It is therefore essential to identify the minimum supercell size that yields a stable interfacial energy.

To this end, calculations were carried out using supercells containing 8, 16, 24, 32, and 40 atoms. Only Ni_3Al precipitate could be used to perform these calculations due to limitations in computational time. This set of calculations using

Ni_3Al was set to be used as a reference to other calculations involving elements like Ti. As it will be discussed, calculations with the other elements could not be performed since energy convergence was not achieved. To determine the optimal supercell size, calculations employing pure Ni as the matrix phase and Ni_3Al as the $L1_2$ precipitate phase were made. Figure 3.17 illustrates an example of the supercells used for interfacial energy calculations, specifically for the case of a system containing 32 atoms.

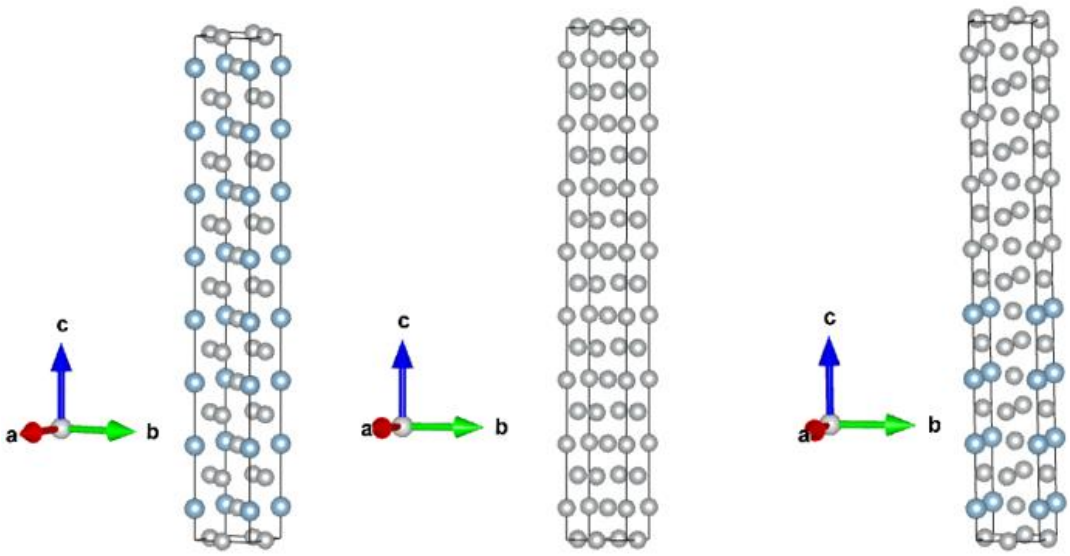

Figure 3.17: Supercells prototypes to perform DFT calculations for accessing interfacial energies. In left, pure precipitate. In the middle, pure FCC matrix and in the right side, the mixed structure containing the interface.

The main limitation of the adopted approach is that convergence of the interfacial energy could not be achieved within the range of supercell sizes considered. The corresponding results are summarized in Table 3.4.

As shown in the table, increasing the number of atoms in the system leads to a continuous decrease in the calculated interfacial energy. This behavior deviates from what is typically expected in a convergence analysis, where the energy would stabilize around an intermediate value as the system size increases. Moreover, when supercells containing 32 atoms are employed, the calculated interfacial energy becomes negative, which is inconsistent with the physical expectation for an interfacial energy.

Interestingly, when supercells containing 40 atoms are considered, a change in the trend is observed, suggesting that the interfacial energy may begin to increase for systems larger than 40 atoms. However, due to limitations in computational resources and time, calculations involving supercells with more than 40 atoms could not be performed. Consequently, the alternative approach described in Section 3.3.5 was adopted to estimate the interfacial energies.

Table 3.4: dependence of interfacial energies and size of the unit cells used to emulate the interfaces between FCC Ni and $L1_2$ Ni_3Al

Number of atoms in the system	Interfacial energy (mJ/m2)
8	63.0
16	24.4
24	10.8
32	-21.3
40	-14.9

One possible explanation for the nonphysical results obtained in the interfacial energy calculations is that the adopted computational approach may not be the most suitable for the metallic system investigated. As discussed previously, different formulations can be employed to compute interfacial energies. Vitos et al. [97] point out that calculating interfacial energies directly from the total energies of supercells containing the pure precipitate, the pure matrix, and their combined system may introduce significant errors.

This issue arises from the periodic repetition of multilayer supercells. Such effects are discussed in detail by Boettger et al. [98], who demonstrated that, in thin-film calculations, the simulation error increases linearly with supercell thickness. According to Boettger, when the system is effectively treated as a bulk material, the resulting error can become substantial, leading to unphysical results. This perspective suggests that, to properly model an interface—conceptually analogous to a thin film—it is necessary to explicitly introduce vacuum regions rather than relying on bulk-like supercells. Consequently, additional modifications to the interfacial energy calculation methodology are required beyond simply combining the total energies of separate supercells. Both

Vitos et al. [97] and Boettger et al. [98] propose that the energies of the individual phases (pure matrix and pure precipitate) should be determined using an incremental approach.

In this approach, a supercell containing a single phase, for example Ni_3Al, is first constructed and its total energy is calculated. Subsequently, one additional unit cell is appended to the supercell, and the total energy is recalculated. The difference between these two energies corresponds to the incremental energy of the added unit cell. This procedure is repeated until the incremental energy converges to a stable value. Once convergence is achieved, this incremental energy is taken as the representative bulk energy per unit cell for that phase. The total bulk energy used in the interfacial energy calculation is then obtained by multiplying this incremental energy by the number of unit cells of the corresponding phase present in the interfacial supercell. This procedure is applied independently to both phases in the system.

Using this methodology, the final expression for the interfacial energy assumes the form given in Eq. 7. In that equation $E_{Ni + Ni3Al}$ is the energy of the supercell containing both phases pure Ni and $L1_2$ Ni_3Al phases. E Bulk Strained, Ni is the incremental energy obtained for pure Ni and E Bulk Ni3Al the incremental energy calculated for that phase. M and N are the numbers of unit cells for each phase used to construct their respective supercell. A is the area of the interface between the two phases. The term “strained” associated with Ni reflects the fact that this methodology adopts the larger lattice parameter of the two phases for constructing all supercells. Therefore, pure Ni experiences elastic strain due to the imposed lattice parameter.

This supercell construction strategy differs from that employed in the present work, in which the lattice parameter used for all calculations was taken as the arithmetic average of the relaxed lattice parameters of pure FCC Ni and pure $L1_2$ Ni_3Al. As a result, the strain state imposed on the phases in the present simulations differs from that described in the incremental-energy methodology discussed above.

$$E_{int} = \frac{E_{Ni+Ni3Al} - 4N\, E^{Bulk}_{Strained,Ni} - 4M\, E^{Bulk}_{Ni3Al}}{2A} \qquad \text{Equation 7}$$

Another significant difference between the methodology employed by Vitos et al. [97,99] and the approach adopted in the present work, which may help explain the observed results, is the inclusion of vacuum regions in the supercells. The presence of vacuum layers serves to separate periodic images of the interfaces, thereby better approximating a thin-film configuration and minimizing errors associated with the periodic repetition of multiple material layers [98].

Due to limitations in computational resources and time, the alternative approaches for interfacial energy calculations discussed in this section could not be implemented in the present study. These methodologies are therefore suggested as promising directions for future work.

3.4.2 ANALYSIS OF SYNCHROTRON SINGLE SHOTS

As an alternative route to determine the interfacial energy of the $L1_2$/FCC interface, an additional method was employed based on the analysis of synchrotron X-ray diffraction data. This approach enables the estimation of the volume fraction of a given phase as a function of time and/or temperature.

Figure 3.18 illustrates three distinct heat-treatment stages applied to the material. The H1 curve corresponds to the initial heating cycle, during which the precipitate volume fraction increases from approximately 5% to about 10%. Subsequently, the precipitates dissolve, and upon cooling, the $L1_2$ phase is not detected until the temperature decreases to approximately 915 °C. As the temperature continues to decrease, as shown by the C1 curve corresponding to the cooling stage, the precipitate volume fraction increases from 0% to values exceeding 20%.

A second heating cycle, represented by the H2 curve, follows the cooling stage. During this cycle, the $L1_2$ volume fraction established at the end of the C1 stage remains close to 25%, decreasing only slightly as the temperature

increases. An alternative representation of the thermal cycles described in Figure 3.18 is provided in Figure 3.19.

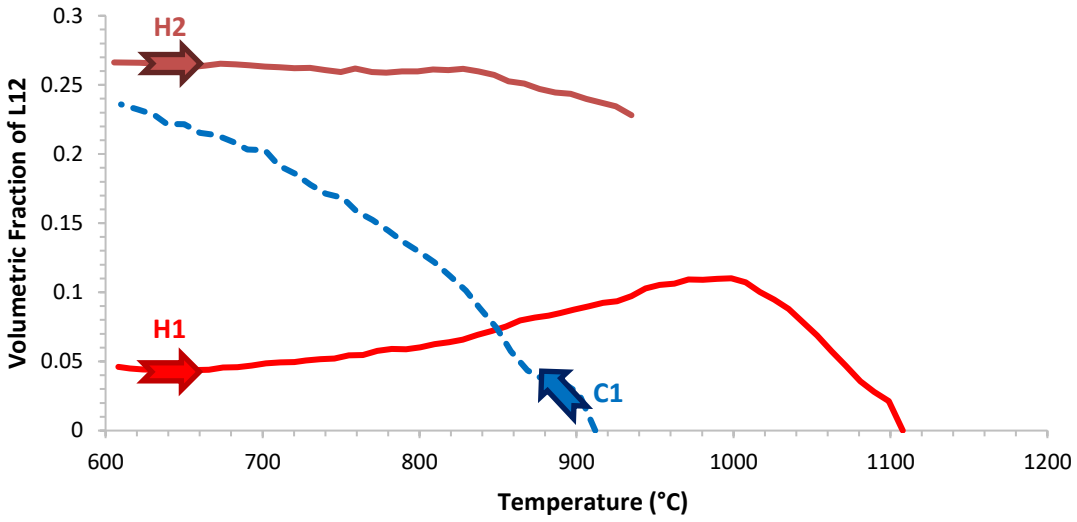

Figure 3.18: Evolution of L12 precipitate volumetric fraction related to temperature.

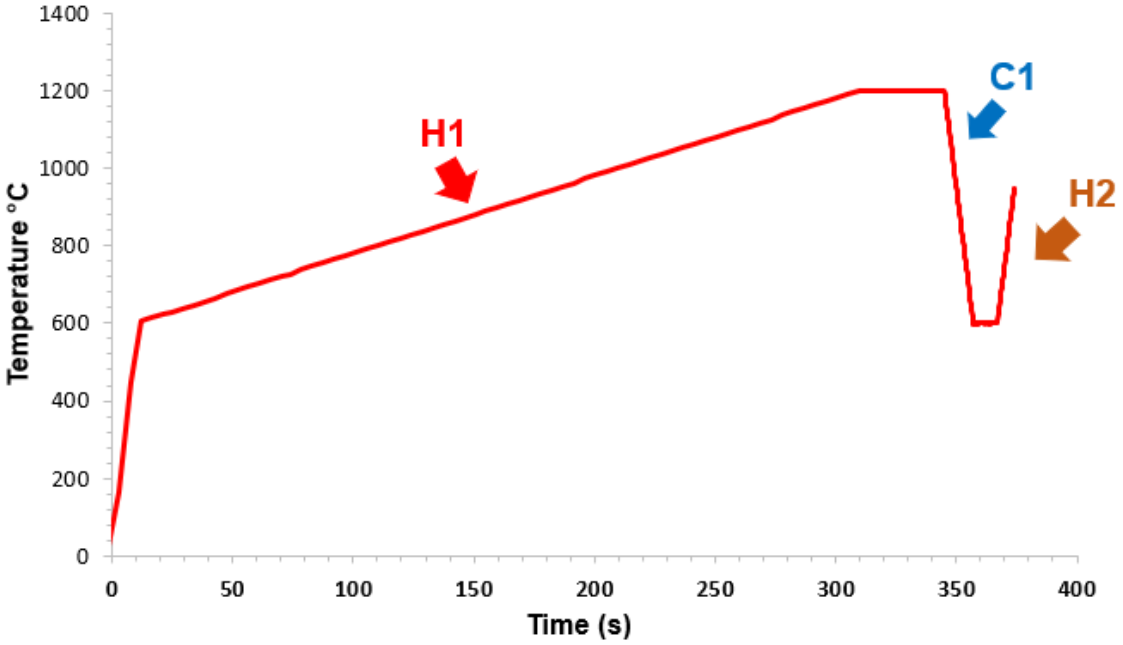

Figure 3.19: Thermal cycles during the synchrotron analysis.

The volume fraction of the $L1_2$ phase was determined from the synchrotron X-ray diffraction (S-XRD) patterns using Equation 8. In this expression, A represents the experimentally integrated intensity of a given (hkl) reflection, defined as the area under the corresponding diffraction peak; I denote the theoretical relative integrated intensity of the (hkl) reflection (given by Equation 9); and n is the number of diffraction peaks considered in the analysis.

The theoretical relative integrated intensity (I) was calculated using Equation 2, where V is the unit-cell volume (m^3), |F| is the structure factor, p is the multiplicity factor, and the term in parentheses corresponds to the Lorentz–polarization factor, which depends on the diffraction angle (θ).

$$f_{L12} = \frac{\frac{1}{n}\sum_{j=1}^{n}\frac{A_{L12}^{j}}{I_{L12}^{j}}}{\frac{1}{n}\sum_{j=1}^{n}\frac{A_{L12}^{j}}{I_{L12}^{j}} + \frac{1}{n}\sum_{j=1}^{n}\frac{A_{FCC}^{j}}{I_{FCC}^{j}}} \quad \text{Eq. 8}$$

$$I = \left(\frac{1}{V^2}\right)|F|^2 p\left(\frac{1+cos^2 2\theta}{sin^2\theta\ cos\theta}\right) \quad \text{Eq. 9}$$

3.4.3 PRECIPITATION SIMULATIONS

The results of the simulations relating the $L1_2$ volume fraction in the FCC matrix to the interfacial energy between the two phases are presented in Figure 3.20. It can be observed that, as the interfacial energy increases, the volume fraction of the $L1_2$ phase decreases, reaching zero when the interfacial energy (*E*_{int}) is approximately 75 $mJ \cdot m^{-2}$. When the interfacial energy is around 50 $mJ \cdot m^{-2}$, the predicted volume fraction of the γ′ phase closely matches the value obtained from the synchrotron diffraction analyses described in Section 3.5.2.

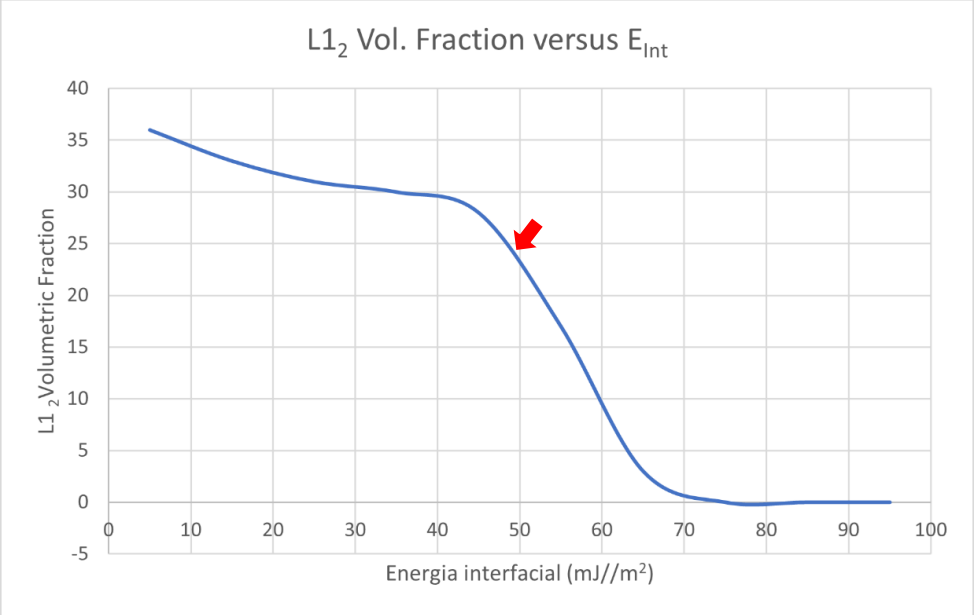

Figure 3.20: Changes in the volume fraction of $L1_2$ as the interfacial energy is changed in precipitation simulations.

Interestingly, the value of approximately 50 mJ·m^{-2} is close to that adopted by Santana et al. when simulating precipitate size distributions (PSDs) for a different high-entropy alloy. In that study, an interfacial energy of about 48 mJ·m^{-2} was required to obtain good agreement between CALPHAD-based PSD simulations and previously reported experimental data. When a lower value of 15 mJ·m^{-2} was used in those simulations, the difference between the peak positions of the experimental and simulated PSDs was approximately 33%.

Similarly, when the same interfacial energy value of 15 mJ·m^{-2} is used to estimate phase volume fractions, the agreement deteriorates, with a difference of about 37.5% between experimental and simulated results. Although these observations do not allow one to establish a clear linear relationship between the interfacial energy and the discrepancy between simulated and experimental precipitate characteristics, it is noteworthy that, in both cases, interfacial energy values close to 50 mJ·m^{-2} lead to significantly improved agreement. This trend is observed for both the HEA investigated in the present work and the alloy reported in the literature.

When compared with the results obtained using the semi-empirical approach described earlier, these findings suggest that the interfacial energy of

the alloy studied here is on the order of 50 $mJ \cdot m^{-2}$. This magnitude is reasonable for Ni-based alloys. For instance, reported interfacial energies between an FCC matrix and the γ″ phase is of the same order of magnitude. Several ab initio studies report values such as 49, 61, and 48 $mJ \cdot m^{-2}$ [99–101].

It is also important to note that additional factors may influence DFT-based interfacial energy calculations, such as the c/a ratio of the supercells and the distance between interfaces, both of which can be affected by magnetic effects. It has been shown that modifying these parameters in DFT calculations performed with VASP—while keeping all other settings unchanged except for the treatment of magnetism—can lead to variations in the calculated interfacial energy of up to 40 $mJ \cdot m^{-2}$, and may even result in negative values (e.g., −39 $mJ \cdot m^{-2}$) [96].

3.5 CONCLUSIONS

A high-entropy alloy was designed using high-throughput thermodynamic calculations. DFT simulations were subsequently performed to investigate this alloy with respect to the interfacial energy between its FCC matrix and $L1_2$ γ′ precipitates, with the objective of employing the calculated values as input parameters for thermodynamic and kinetic simulations.

The analyses yielded noteworthy results. Although some of the interfacial energies calculated using DFT were not physically reasonable for the alloy studied, the results demonstrate that the proposed methodology is capable of providing valuable insights. With further refinement and methodological adaptations, this simulation framework may, in future studies, achieve the initial objectives of the work more effectively.

In addition to the DFT analysis, a semi-empirical approach was employed to estimate the interfacial energy between the matrix and γ′ precipitates. In this methodology, the material was subjected to synchrotron X-ray diffraction, and the resulting data were used to establish a quantitative relationship between time, temperature, and the volume fraction of the γ′ phase within the FCC matrix. These experimental results were then used as a reference for precipitation simulations

performed using Pandat®, in which the interfacial energy was systematically varied while reproducing the same thermal treatments applied experimentally.

The simulations revealed a clear dependence of the $L1_2$ volume fraction on the assumed interfacial energy. By comparing experimental and simulated results, the interfacial energy value that provided the best agreement was found to be approximately 50 $mJ \cdot m^{-2}$. This value is physically reasonable for coherent interfaces in the context of both high-entropy alloys and Ni-based superalloys. These findings demonstrate that the combination of precipitation simulations with the adopted experimental methodology can yield meaningful insights into interfacial phenomena.

Finally, the integration of this semi-empirical approach with improved DFT-based calculations holds significant potential for the development of robust methodologies capable of reliably estimating interfacial energies between constituents of complex metallic systems.

CHAPTER 4 – FINAL DISCUSSION AND CONCLUSIONS

4.1 CONCLUSIONS

This work investigated multiphase, multi-principal-element alloys through a combination of experimental processing, microstructural characterization, and computational modeling. Two complementary approaches were adopted to enhance the understanding of strengthening and stability mechanisms in complex concentrated alloys.

In the first part, a Cr–Co–Ni-based duplex alloy containing FCC and BCC phases was designed. CALPHAD simulations identified a composition capable of stabilizing a dual-phase microstructure while suppressing σ-phase formation. Experimental results confirmed the presence of FCC and BCC microconstituents in the as-cast condition; however, σ-phase precipitation was observed after homogenization, revealing limitations in the current thermodynamic databases for this alloy system. Despite this deviation, nanoindentation measurements demonstrated promising mechanical behavior within the duplex regions, where a tough, low–stacking-fault-energy FCC matrix coexisted with a stronger Cr-rich BCC phase. These results indicate that carefully engineered Cr–Co–Ni duplex compositions, when optimized to suppress σ-phase formation, can provide a synergistic balance of strength and ductility.

In the second part of the study, a precipitation-strengthened high-entropy alloy containing nanometric $L1_2$-type precipitates was examined. A combined first principles and CALPHAD-based strategy was employed to determine the interfacial energies between the matrix and precipitates. DFT simulations were carried out to obtain reliable energetic parameters, which were subsequently used as inputs for kinetic precipitation models. This approach demonstrated the effectiveness of integrating ab initio methods with thermodynamic calculations to predict microstructural evolution in chemically complex alloys, thereby supporting the rational design of HEAs and HESAs.

Overall, the results reinforce that multiphase alloy design represents a promising pathway for advancing HEA technology. Duplex and precipitation strengthened HEAs can achieve mechanical performance comparable to, or exceeding, that of conventional superalloys and advanced steels, provided that

phase stability is accurately predicted and controlled. The observed limitations of existing thermodynamic databases underscore the ongoing need for experimental validation and for incorporating first-principles data to refine phase stability descriptions in HEAs. In particular, the methodologies adopted in the second part of this work—combining CALPHAD, DFT, and advanced characterization techniques—constitute a robust framework for future alloy development, owing to their ability to access fundamental quantities such as interfacial energies involving key microstructural constituents.

4.2 SUGGESTIONS FOR FUTURE WORKS

As demonstrated in this work, research focused on multiphase high-entropy alloys (HEAs), as well as the simulation of metallic alloy properties, still offers substantial opportunities for further improvement. Several promising directions for future research can be identified:

Regarding chapter 2: Future studies involving additional mechanical testing of the Cr–Co–Ni alloy, such as tensile testing and complementary mechanical characterization techniques, would be valuable for achieving a more comprehensive understanding of its mechanical behavior. Moreover, further investigations into the performance of CALPHAD thermodynamic databases for this alloy system are warranted. In particular, identifying the database that most accurately describes the phase stability of the $Cr_{33.5}Co_{15}Ni_{51.5}$ alloy would be of significant interest. Another relevant topic for future research is the clarification of why Tsai's criteria do not align with the phase predictions obtained using the database employed in Chapter 2. In addition, the production and analysis of additional alloy compositions could be pursued to investigate strategies for mitigating σ-phase formation, for example by reducing the cobalt content.

Regarding chapter 3: Several additional research avenues can also be explored. One possibility is the application of alternative computational methods and software packages for calculating interfacial energies, as reported in other studies. Such analyses were not conducted in the present work due to limitations in computational resources and software availability. Comparative studies of

different DFT codes could help identify which approaches yield the most reliable interfacial energy predictions for the systems investigated here. Another promising direction is the explicit inclusion of vacuum layers in the supercell models to better isolate interfaces, an approach that has been successfully applied in previous studies and may provide new insights for metallic systems related to HEAs. Furthermore, extended experimental characterization of the alloy would be highly beneficial. Additional measurements of the $L1_2$ volume fraction as a function of temperature or time, obtained via synchrotron X-ray diffraction, could supply further datasets for fitting and enable more robust comparisons with computational predictions.

REFERENCES

[1] Coury, Francisco G., Guilherme Zepon, and Claudemiro Bolfarini. - Multi-Principal Element Alloys from the CrCoNi Family: Outlook and Perspectives.Journal of materials research and technology 15 (2021)

[2] Cheng, Chun-Yang et al. - Physical Metallurgy of Concentrated Solid Solutions from Low-Entropy to High-Entropy Alloys. Current opinion in solid state & materials science 21.6 (2017).

[3] Jien-Wei Yeh, Swe-Kai Chen, Su-Jien Lin, Jon-Yiew Gan, Tsung-Shune Chin, Tao-Tsung Shun, Chun-Huei Tsau, and Shou-Yi Chang - Nanostructured High-Entropy Alloys with Multiple Principal Elements: Novel Alloy Design Concepts and Outcomes

[4] CANTOR, B. et al. Microstructural development in equiatomic multicomponent alloys. Materials Science and Engineering A, v. 375, p. 213–218, 2004. Disponível em: http://dx.doi.org/10.1016/j.msea.2003.10.257

[5] Miracle, D.B., and O.N. Senkov. - A Critical Review of High Entropy Alloys and Related Concepts. Acta materialia 122 (2017).

[6] Xin-Wei Yang, Xiao-Hui Shi, Hui-Jun Yang, Jun-Wei Qiao, Peter K. Liaw, Yu-Cheng Wu - Entropy versus enthalpy in hexagonal-close-packed high entropy alloys

[7] Jien-Wei Yeh1, Yu-Liang Chen1, Su-Jien Lin and Swe-Kai Chen - HIGH-ENTROPY ALLOYS – A New Era of Exploitation

[8] Dong Liu, Qin Yu, Saurabh Kabra, Ming Jiang, Paul Forna-Kreutzer, Ruopeng Zhang, Madelyn Payne, Flynn Walsh, Bernd Gludovatz, Mark Asta, Andrew M. Minor, Easo P. George, Robert O. Ritchie - Exceptional fracture toughness of CrCoNi-based medium- and high-entropy alloys at 20 kelvin.

[9] F. Otto, A. Dlouhý, Ch. Somsen, H. Bei, G. Eggeler, E.P. George, The influences of temperature and microstructure on the tensile properties of a CoCrFeMnNi high-entropy alloy, Acta Materialia, Volume 61, Issue 15,

2013, Pages 5743-5755, ISSN 1359-6454, https://doi.org/10.1016/j.actamat.2013.06.018.

[10] S.S. Nene, M. Frank, K. Liu, S. Sinha, R.S. Mishra, B.A. McWilliams, K.C. Cho, Corrosion-resistant high entropy alloy with high strength and ductility, Scripta Materialia, Volume 166, 2019, Pages 168-172, ISSN 1359-6462, https://doi.org/10.1016/j.scriptamat.2019.03.028.

[11] Xie, X., Li, N., Liu, W. et al. Research Progress of Refractory High Entropy Alloys: A Review. Chin. J. Mech. Eng. 35, 142 (2022). https://doi.org/10.1186/s10033-022-00814-0

[12] László Bencze, Georg Hasemann, Dmitry Sergeev, Vladimir Motalov, Michael Müller, Manja Krüger, Thermodynamic properties of refractory Mo-Nb-V-Ti high entropy alloys (HEAs), Journal of Alloys and Compounds, Volume 976, 2024, 173279, ISSN 0925-8388, https://doi.org/10.1016/j.jallcom.2023.173279.

[13] Jiro Kitagawa, Shusuke Hamamoto and Naoki Ishizu - Cutting Edge of High-Entropy Alloy Superconductors from the Perspective of Materials Research.

[14] Bin Liu, Jifeng Wu, Yanwei Cui, Qinqing Zhu, Guorui Xiao, Siqi Wu, Guanghan Cao, Zhi Ren, Superconductivity in hexagonal Nb-Mo-Ru-Rh-Pd high-entropy alloys, Scripta Materialia, Volume 182, 2020, Pages 109-113, ISSN 1359-6462, https://doi.org/10.1016/j.scriptamat.2020.03.004.

[15] Moses A. Adaan-Nyiak, Intekhab Alam, Ahmed A. Tiamiyu, Ball milling process variables optimization for high-entropy alloy development using design of experiment and genetic algorithm, Powder Technology, Volume 427, 2023, 118766, ISSN 0032-5910, https://doi.org/10.1016/j.powtec.2023.118766.

[16] Vishnu Raghuraman, Yang Wang, Michael Widom; An investigation of high entropy alloy conductivity using first-principles calculations. Appl. Phys. Lett. 20 September 2021; 119 (12): 121903. https://doi.org/10.1063/5.0065239

[17] Liu, Z., Lei, Y., Gray, C. et al. Examination of Solid-Solution Phase Formation Rules for High Entropy Alloys from Atomistic Monte Carlo Simulations. JOM 67, 2364–2374 (2015). https://doi.org/10.1007/s11837-015-1508-3

[18] Yihan Niu, Dan Zhao, Bo Zhu, Shunbo Wang, Zhaoxin Wang, Hongwei Zhao, Investigations on the role of chemical short-range order in the tensile deformation of FCC Co30Fe16.67Ni36.67Ti16.67 high-entropy alloys via Monte Carlo and molecular dynamics hybrid simulations, Computational Materials Science, Volume 215, 2022, 111787, ISSN 0927-0256, https://doi.org/10.1016/j.commatsci.2022.111787.

[19] Barnasree Chanda, Parijat P. Jana, Jayanta Das, A tool to predict the evolution of phase and Young's modulus in high entropy alloys using artificial neural network, Computational Materials Science, Volume 197, 2021, 110619, ISSN 0927-0256, https://doi.org/10.1016/j.commatsci.2021.110619.

[20] Shuai Li, Shu Li, Dongrong Liu, Rui Zou, Zhiyuan Yang, Hardness prediction of high entropy alloys with machine learning and material descriptors selection by improved genetic algorithm, Computational Materials Science, Volume 205, 2022, 111185, ISSN 0927-0256, https://doi.org/10.1016/j.commatsci.2022.111185.

[21] Zhang, Yiqiong & Wang, Dongdong & Wang, Shuangyin. (2021). High-Entropy Alloys for Electrocatalysis: Design, Characterization, and Applications. Small. 18. 2104339. 10.1002/smll.202104339.

[22] Michael Moschetti, Patrick A. Burr, Edward Obbard, Jamie J. Kruzic, Peter Hosemann, Bernd Gludovatz, Design considerations for high entropy alloys in advanced nuclear applications, Journal of Nuclear Materials, Volume 567, 2022, 153814, ISSN 0022-3115, https://doi.org/10.1016/j.jnucmat.2022.153814.

[23] Shao-Ping Wang, Jian Xu, TiZrNbTaMo high-entropy alloy designed for orthopedic implants: As-cast microstructure and mechanical properties, Materials Science and Engineering: C, Volume 73, 2017, Pages 80-89, ISSN 0928-4931, https://doi.org/10.1016/j.msec.2016.12.057.

[24] Chrzan Konrad, Cichocki Kamil, Adamczyk Piotr, Drozdz Paweł, Kozieł Tomasz, Bała Piotr, Muszka Krzysztof - Assessment of utilization of ab-initio and Calphad calculations for a design of high-entropy alloy for metal forming, 18th International Conference Metal Forming 2020.

[25] Gludovatz, B., Hohenwarter, A., Thurston, K. et al. Exceptional damage-tolerance of a medium-entropy alloy CrCoNi at cryogenic temperatures. Nat Commun 7, 10602 (2016). https://doi.org/10.1038/ncomms10602

[26] Francisco Gil Coury, Diego Santana, Yaofeng Guo, John Copley, Lucas Otani, Solange Fonseca, Guilherme Zepon, Claudio Kiminami, Michael Kaufman, Amy Clarke, Design and in-situ characterization of a strong and ductile co-rich multicomponent alloy with transformation induced plasticity, Scripta Materialia, Volume 173, 2019, Pages 70-74, ISSN 1359-6462, https://doi.org/10.1016/j.scriptamat.2019.07.045.

[27] N. Haghdadi, S. Primig, M. Annasamy, P. Cizek, P.D. Hodgson, D.M. Fabijanic, Dynamic recrystallization in AlXCoCrFeNi duplex high entropy alloys, Journal of Alloys and Compounds, Volume 830, 2020, 154720, ISSN 0925-8388, https://doi.org/10.1016/j.jallcom.2020.154720.

[28] Wei Wang, Yong Wang, Wangzhong Mu, Joo Hyun Park, Hui Kong, Sohei Sukenaga, Hiroyuki Shibata, Henrik Larsson, Huahai Mao, Inclusion engineering in Co-based duplex entropic alloys, Materials & Design, Volume 210, 2021, 110097, ISSN 0264-1275, https://doi.org/10.1016/j.matdes.2021.110097.

[29] Ka Ram Lim, Heoun Jun Kwon, Joo-Hee Kang, Jong Woo Won, Young Sang Na, A novel ultra-high-strength duplex Al–Co–Cr–Fe–Ni high-entropy alloy reinforced with body-centered-cubic ordered-phase particles, Materials

Science and Engineering: A, Volume 771, 2020, 138638, ISSN 0921-5093, https://doi.org/10.1016/j.msea.2019.138638.

[30] Ming-Hung Tsai, Kun-Yo Tsai, Che-Wei Tsai, Chi Lee, Chien-Chang Juan & Jien-Wei Yeh (2013) Criterion for Sigma Phase Formation in Cr- and V-Containing High Entropy Alloys, Materials Research Letters, 1:4, 207-212, DOI: 10.1080/21663831.2013.831382

[31] Ming-Hung Tsai, Keng-Che Chang, Jian-Hong Li, Ruei-Chi Tsai & An-Hung Cheng (2016) A second criterion for sigma phase formation in high-entropy alloys, Materials Research Letters, 4:2, 90-95, DOI: 10.1080/21663831.2015.1121168

[32] Oliver, W. C., & Pharr, G. M. (1992). An improved technique for determining hardness and elastic modulus using load and displacement sensing indentation experiments.

[33] Qiao, P., Xie, J., Jiang, Y., Tang, P., Liang, B., Lu, Y., & Gong, J. (2022). Mechanical Properties of σ-Phase and Its Effect on the Mechanical Properties of Austenitic Stainless Steel. Coatings, 12(12). https://doi.org/10.3390/coatings12121917

[34] Gao, X. L., Jing, X. N., & Subhash, G. (2006). Two new expanding cavity models for indentation deformations of elastic strain-hardening materials. International Journal of Solids and Structures, 43(7–8), 2193–2208. https://doi.org/10.1016/j.ijsolstr.2005.03.062

[35] Bertoli, G., Otani, L. B., Clarke, A. J., Kiminami, C. S., & Coury, F. G. (2021). Hall-Petch and grain growth kinetics of the low stacking fault energy TRIP Cr40Co40Ni20 multi-principal element alloy. Applied Physics Letters, 119(6). https://doi.org/10.1063/5.0057888

[36] Wu, Z., Bei, H., Pharr, G. M., & George, E. P. (2014). Temperature dependence of the mechanical properties of equiatomic solid solution alloys with face-centered cubic crystal structures. Acta Materialia, 81, 428–441. https://doi.org/10.1016/j.actamat.2014.08.026

[37] W. Lu, X. Luo, Y. Yang, J. Zhang, B. Huang, Mater. Chem. Phys. 2019, 238, 121841.

[38] J. Ruud, United States Patent : 3871965 United States Patent : 3871965. Yeast. 2, 4–6 (2010).

[39] Stephens, J. R., & Kzopp, W. D. (n.d.). NASA TECHNICAL NOTE - DUCTILITY MECHANISMS AND SUPERPLASTICITY I N CHROMIUM ALLOYS.

[40] Bertoli, G., de Sousa, V. G. L., de A. Santana, D., Otani, L. B., Kiminami, C. S., & Coury, F. G. (2022). Phase equilibria of VCrMnFeCo high entropy alloys. Journal of Alloys and Compounds, 903. https://doi.org/10.1016/j.jallcom.2022.163950

[41] Coury, F. G., Kaufman, M., & Clarke, A. J. (2019). Solid-solution strengthening in refractory high entropy alloys. Acta Materialia, 175, 66–81. https://doi.org/10.1016/j.actamat.2019.06.006

[42] Joele, M., & Matizamhuka, W. R. (2021). A review on the high temperature strengthening mechanisms of high entropy superalloys (Hesa). In Materials (Vol. 14, Issue 19). MDPI. https://doi.org/10.3390/ma14195835

[43] Sousa, I. S. (2009). UNIVERSIDADE FEDERAL DO ESPÍRITO SANTO CENTRO TECNOLÓGICO DEPARTAMENTO DE ENGENHARIA MECÂNICA PROJETO DE GRADUAÇÃO A INFLUÊNCIA DO TRATAMENTO TÉRMICO DE ENVELHECIMENTO NA DUREZA DA SUPERLIGA DE NÍQUEL INCONEL 625

[44] Design of Modern High Nb-Content γ-γ’ Ni-Base Superalloys

[45] R. C. Reed, The Superalloys Fundamentals and Applications. Cambridge University Press, 2006.

[46] Santana, D. A., Santos, K. R., Kiminami, C. S., & Coury, F. G. (2021). Design, phase equilibria, and coarsening kinetics of a new γ/γ′ precipitation-

hardened multi-principal element alloy. Journal of Alloys and Compounds, 882. https://doi.org/10.1016/j.jallcom.2021.160729

[47] Cahn JW, Hilliard JE. J Chem Phys 1958;28:258

[48] Heshmati, M., Haghani, R., & Al-Emrani, M. (2015). Environmental durability of adhesively bonded FRP/steel joints in civil engineering applications: State of the art. Composites Part B: Engineering, 81, 259–275. https://doi.org/10.1016/j.compositesb.2015.07.01450

[49] Xu, Y., Li, Y., Chen, T., Dong, C., Zhang, K., & Bao, X. (2024). A short review of medical-grade stainless steel: Corrosion resistance and novel techniques. Journal of Materials Research and Technology, 29, 2788–2798. https://doi.org/10.1016/j.jmrt.2024.01.240

[50] Yoo, B., Jung, C., Jang, K., Jun, H., & Choi, P. P. (2024). Novel Ni–Co-based superalloys with high thermal stability and specific yield stress discovered by directed energy deposition. Materials and Design, 238. https://doi.org/10.1016/j.matdes.2023.112607

[51] Eliaz, N., Shemesh, G., & Latanision, R. M. (n.d.). Hot corrosion in gas turbine components. www.elsevier.com/locate/engfailanal

[52] Lemos, G. (n.d.). Development of Ni-based Superalloy Metal Matrix Composites, Featuring High Creep Resistance.

[53] Kanesund, J., Brodin, H., & Johansson, S. (2020). High temperature corrosion influence on deformation and damage mechanisms in turbine blades made of IN-792 during service. Engineering Failure Analysis, 110. https://doi.org/10.1016/j.engfailanal.2020.104388

[54] Luiss, A. P., & Carli, G. (n.d.). Divide and rule : firm boundaries in the aircraft engine industry. https://www.researchgate.net/publication/33775942

[55] He, L. Z., Zheng, Q., Sun, X. F., Guan, H. R., Hu, Z. Q., Tieu, A. K., Lu, C., & Zhu, H. T. (2005). Effect of carbides on the creep properties of a Ni-base

superalloy M963. Materials Science and Engineering: A, 397(1–2), 297–304. https://doi.org/10.1016/j.msea.2005.02.038

51

[56] Claudia, A., Hirschmann, O., de Moura Neto, C., & Reis, D. A. (n.d.). FUNDAMENTOS BÁSICOS SOBRE SUPERLIGAS - BASIC FUNDAMENTAL OF SUPERALLOYS.

[57] Chen, Y. T., Chang, Y. J., Murakami, H., Gorsse, S., & Yeh, A. C. (2020). Designing high entropy superalloys for elevated temperature application. Scripta Materialia, 187, 177–182. https://doi.org/10.1016/j.scriptamat.2020.06.002

[58] Basu, I.; De Hosson, J.T. Strengthening mechanisms in high entropy alloys: Fundamental issues. Scr. Mater. 2020, 187, 148–156.

[59] R.E. Smallman CBE, DSc, FRS, FREng, FIM, R.J. Bishop PhD, CEng, MIM, in Modern Physical Metallurgy and Materials Engineering (Sixth Edition), 1999Chapter 4 Defects in solids 4.1 Types of imperfection. (n.d.).

[60] Zhang, P., Yuan, Y., Li, J., Xu, Y. F., Song, X. L., & Yang, G. X. (2017). Tensile deformation mechanisms in a new directionally solidified Ni-base superalloy containing coarse γ′ precipitates at 650 °C. Materials Science and Engineering: A, 702, 343–349. https://doi.org/10.1016/j.msea.2017.07.025

[61] Dodaran, M., Ettefagh, A. H., Guo, S. M., Khonsari, M. M., Meng, W. J., Shamsaei, N., & Shao, S. (2020). Effect of alloying elements on the γ' antiphase boundary energy in Ni-base superalloys. Intermetallics, 117. https://doi.org/10.1016/j.intermet.2019.106670

[62] Collins, D. M., & Stone, H. J. (2014). A modelling approach to yield strength optimisation in a nickel-base superalloy. International Journal of Plasticity, 54, 96–112. https://doi.org/10.1016/j.ijplas.2013.08.00952

[63] Kozar, R. W., Suzuki, A., Milligan, W. W., Schirra, J. J., Savage, M. F., & Pollock, T. M. (2009). Strengthening mechanisms in polycrystalline multimodal nickel-base superalloys. Metallurgical and Materials Transactions A: Physical Metallurgy and Materials Science, 40(7), 1588–1603. https://doi.org/10.1007/s11661-009-9858-5

[64] Ruzic, J., Goto, K., Watanabe, I., Osada, T., Wu, L., & Ohmura, T. (2021). Temperature-dependent deformation behavior of γ and γ′ single-phase nickel-based superalloys. Materials Science and Engineering: A, 818. https://doi.org/10.1016/j.msea.2021.141439

[65] Rakoczy, L., Milkovic, O., Rutkowski, B., Cygan, R., Grudzien-Rakoczy, M., Kromka, F., & Zielinska-Lipiec, A. (2020). Characterization of γ' precipitates in cast NiBased superalloy and their behaviour at high-homologous temperatures studied by TEM and in situ XRD. Materials, 13(10). https://doi.org/10.3390/ma13102397

[66] Gleeson, B., Mu, N., & Hayashi, S. (2009). Compositional factors affecting the establishment and maintenance of Al2O3 scales on Ni-Al-Pt systems. Journal of Materials Science, 44(7), 1704–1710. https://doi.org/10.1007/s10853-009-3251-z

[67] Kaptay, G. (2012). On the interfacial energy of coherent interfaces. Acta Materialia, 60(19), 6804–6813. https://doi.org/10.1016/j.actamat.2012.09.002

[68] Wu, X. (2019). Deformation and Evolution of Life in Crystalline Materials. In Deformation and Evolution of Life in Crystalline Materials. CRC Press. https://doi.org/10.1201/b22348

[69] Devaux, A., Nazé, L., Molins, R., Pineau, A., Organista, A., Guédou, J. Y., Uginet, J. F., & Héritier, P. (2008). Gamma double prime precipitation kinetic in Alloy 718. Materials Science and Engineering: A, 486(1–2), 117–122. https://doi.org/10.1016/j.msea.2007.08.04653

[70] A. K. Sinha, Topologically close-packed structures of transition metal alloys, Progress in Materials Science, 15 (1972), 79–185.

[71] I. Lifshitz and V. Slyozov, “The kinetics of precipitation from supersaturated solid solutions,” Journal of Physics and Chemistry of Solids, vol. 19, pp. 35–50, apr 1961

[72] C. Wagner, “Theory of precipitate change by redissolution,” Z. Elektrochem, vol. 65, pp. 581–591, 1961.

[73] A. Ardell, “The e↵ect of volume fraction on particle coarsening: theoretical considerations,” Acta Metallurgica, vol. 20, pp. 61–71, jan 1972.

[74] Wang, J., Huang, H., Xin, D., Hu, J., Zhang, H., Ruan, J., Zhou, X., Zhang, S., & Jiang, L. (2024). Dissolution behavior and kinetics of the γ′ precipitates within a novel powder metallurgy Ni-based superalloy. Journal of Materials Research and Technology, 30, 1950–1961. https://doi.org/10.1016/j.jmrt.2024.03.198

[75] Chandran, M., Lee, S. C., & Shim, J. H. (2018). Machine learning assisted firstprinciples calculation of multicomponent solid solutions: Estimation of interface energy in Ni-based superalloys. Modelling and Simulation in Materials Science and Engineering, 26(2). https://doi.org/10.1088/1361-651X/aa9f37

[76] Martinotto, A. L. (n.d.). Universidade Federal do Rio Grande do Sul Programa de Pós-Graduação em Ciência dos Materiais EFEITOS DA APLICAÇÃO DE ALTAS PRESSÕES SOBRE MATERIAIS TERMOELÉTRICOS COM ESTRUTURA DE ESCUTERUDITA.

[77] Liang, S. X., Liu, K. Y., Zhou, Y. X., Yin, L. X., Shi, Y. D., Zheng, L. Y., & Xing, Z. G. (2022). Interfacial energy between γ/γ′ phases of Ni–Al alloys extracted by using a new method. Materials Chemistry and Physics, 277. https://doi.org/10.1016/j.matchemphys.2021.125538

[78] Sonderegger, B., & Kozeschnik, E. (2010). Interfacial energy of diffuse phase boundaries in the generalized broken-bond approach. Metallurgical and Materials.54Transactions A: Physical Metallurgy and Materials Science, 41(12), 3262–3269. https://doi.org/10.1007/s11661-010-0370-8

[79] Ouadah, O., Merad, G., Saidi, F., Mendi, S., & Dergal, M. (2020). Influence of alloying transition metals on structural, elastic, electronic and optical behaviors of γ-TiAl based alloys: A comparative DFT study combined with data mining technique. Materials Chemistry and Physics, 242. https://doi.org/10.1016/j.matchemphys.2019.122455

[80] Gao, L., Song, J., Jiao, Z., Liao, W., Luan, J., Surjadi, J. U., Li, J., Zhang, H., Sun, D., Liu, C. T., & Lu, Y. (2018). High-Entropy Alloy (HEA)-Coated Nanolattice Structures and Their Mechanical Properties. Advanced Engineering Materials, 20(1). https://doi.org/10.1002/adem.201700625

[81] Jo, S., Kim, T., Iyer, V.G., & Im, W. (2008). CHARMM-GUI: A Web-based Graphical User Interface for CHARMM. Journal of Computational Chemistry, 29(11), 1859-1865.

[82] Kresse, G., & Furthmüller, J. (1996). Efficient iterative schemes for ab initio totalenergy calculations using a plane-wave basis set. Physical Review B, 54(16), 11169- 11186

[83] Arnittali, M., Rissanou, A. N., & Harmandaris, V. (2019). Structure of Biomolecules Through Molecular Dynamics Simulations. Procedia Computer Science, 156, 69–78. https://doi.org/10.1016/j.procs.2019.08.181

[84] Janas, A., Piskorz, W., Kryshtal, A., Cempura, G., Belza, W., Kruk, A., Jany, B. R., & Krok, F. (2021). Into the origin of electrical conductivity for the metal– semiconductor junction at the atomic level. Applied Surface Science, 570. https://doi.org/10.1016/j.apsusc.2021.150958

[85] Wang, C., & Wang, C. Y. (2009). Ni/Ni 3 Al interface: A density functional theory study. Applied Surface Science, 255(6), 3669–3675. https://doi.org/10.1016/j.apsusc.2008.10.01755

[86] Wang, J., Yang, X., Zeng, Z., Zhang, X., Zhao, X., & Wang, Z. (2017). New methods for prediction of elastic constants based on density functional theory combined with machine learning. Computational Materials Science, 138, 135–148. https://doi.org/10.1016/j.commatsci.2017.06.015

[87] Zhou, S., Zhang, Y., Jiang, C., & Morgan, D. (2021). A combined ab-initio and empirical model for thermal conductivity of concentrated metal alloys with the focus on binary uranium alloys. Materialia, 15. https://doi.org/10.1016/j.mtla.2020.100990

[88] Hohenberg, P. & Kohn, W. (1964). Inhomogeneous Electron Gas. Physical Review, 136(3B), B864-B871. DOI: 10.1103/PhysRev. 136.B864.

[89] Vanderbilt, D. (n.d.). Rapid Communications Soft self-consistent pseudopotentials in a generalized eigenvalue formalism. In PHYSICAL REVIEW B (Vol. 41).

[90] Ahmed, F. A. M., Xue, H. T., Tang, F. L., An, J. P., Luo, Y. Q., Lu, X. F., & Ren, J. Q. (2020). Segregation of alloying elements and their effects on the thermodynamic stability and fracture strength of γ-Ni/γ′-Ni3Al interface. Journal of Materials Science, 55(26), 12513–12524. https://doi.org/10.1007/s10853-020-04854-6

[91] Bodlos, R., Fotopoulos, V., Spitaler, J., Shluger, A. L., & Romaner, L. (2022). Energies and structures of Cu/Nb and Cu/W interfaces from density functional theory and semi-empirical calculations. Materialia, 21. https://doi.org/10.1016/j.mtla.2022.10136256

[92] Xu, W., Horsfield, A. P., Wearing, D., & Lee, P. D. (n.d.). First-principles calculation of Mg/MgO interfacial free energies.

[93] Li, R., Xie, L., Wang, W. Y., Liaw, P. K., & Zhang, Y. (2020). High-Throughput Calculations for High-Entropy Alloys: A Brief Review. In Frontiers in Materials (Vol. 7). Frontiers Media S.A. https://doi.org/10.3389/fmats.2020.00290

[94] Kundin, J., Mushongera, L., Goehler, T., & Emmerich, H. (2012). Phase-field modeling of the γ′-coarsening behavior in Ni-based superalloys. Acta Materialia, 60(9), 3758–3772. https://doi.org/10.1016/j.actamat.2012.03.023

[95] de Araujo Santana, D., Ellyson, B., Clarke, A., Clarke, K., Schell, N., Kaufman, M., et al. High-throughput strategy to design high entropy alloys with an fcc matrix, l12 precipitates, and optimized yield stress. Materials & Design.2024;244:113173.URL: https://www.sciencedirect.com/science/article/pii/S0264127524005483

[96] Xiong, Z., Li, W., Lu, S., Xu, W., & Vitos, L. (2025). Formation energy of γ/γ″ interfaces in Inconel 718 superalloys. Materials Today Communications, 49. https://doi.org/10.1016/j.mtcomm.2025.114220

[97] Boettger, J. C. (n.d.). Nonconvergence of surface energies obtained from thin-film calculations. In PHYSICAL REVIEW B (Vol. 49).

[98] Lu, S., Zhang, H., Hu, Q. M., Punkkinen, M. P. J., Johansson, B., & Vitos, L. (2014). Magnetic effect on the interfacial energy of the Ni(1 1 1)/Cr(1 1 0) interface. Journal of Physics Condensed Matter, 26(35). https://doi.org/10.1088/0953-8984/26/35/355001

[99] Y. Chen, H. Yu, Y. Chen, H. Di, W. Xu, The strengthening effects and mechanisms of alloying elements on interfaces for multiphase Ni-based superalloys: A firstprinciples study, J. Mater. Res. Technol. 23 (2023) 4802–4813, http://dx.doi. org/10.1016/j.jmrt.2023.02.119.

[100] H. Qin, Z. Bi, H. Yu, G. Feng, J. Du, J. Zhang, Influence of stress on γ'' precipitation behavior in Inconel 718 during aging, J. Alloys Compd. 740 (2018) 997–1006, http://dx.doi.org/10.1016/j.jallcom.2018.01.030.

[101] B.-N. Ngo-Dinh, M. Baeker, Effects of Alloying on the interface energy of the γ''-phase in nickel-based superalloys, Metall. Mater. Trans. A 54 (2023) 1–5, http://dx.doi.org/10.1007/s11661-022-06950-5.

[102] Varvenne, C., Bruneval, F., Marinica, M. C., & Clouet, E. (2013). Point defect modeling in materials: Coupling ab initio and elasticity approaches. Physical Review B - Condensed Matter and Materials Physics, 88(13). https://doi.org/10.1103/PhysRevB.88.134102

[103] Kieffer, J., & Karkoulis, D. (2013). PyFAI, a versatile library for azimuthal regrouping. Journal of Physics: Conference Series, 425(PART 20). https://doi.org/10.1088/1742-6596/425/20/202012